Geochemistry, in-situ Sr-Nd-Hf-O isotopes, and mineralogical constraints on origin and magmatic-hydrothermal evolution of the Yulong porphyry Cu–Mo deposit, Eastern Tibet

Ming-Liang Huang [a, b], Xian-Wu Bi [a, *], Rui-Zhong Hu [a], Jian-Feng Gao [a], Lei-Luo Xu [a], Jing-Jing Zhu [a], Lin-Bo Shang [a]

[a] State Key Laboratory of Ore Deposit Geochemistry, Institute of Geochemistry, Chinese Academy of Sciences, Guiyang 550081, China
[b] University of Chinese Academy of Sciences, Beijing 100049, China

ABSTRACT

The giant Yulong porphyry Cu–Mo deposit was formed in postsubduction setting in eastern Tibet. Origin of the ore-related Yulong intrusion remains a matter of debate. This study presents new whole-rock major and trace element geochemistry, in-situ apatite Sr–Nd and zircon Hf–O isotopes, and mineralogical chemistry of the Yulong intrusion. Least-altered samples from the Yulong intrusion have high SiO_2 (66.3–69.5 wt%) and Al_2O_3 (14.9–15.5 wt%) contents, high La/Yb (36.4–68.0) and Sr/Y (46.0–76.3) ratios, and low MgO (0.63–1.24 wt%) and Cr (<30 ppm) contents, similar to adakitic rocks deriving from thick juvenile lower crust. They are enriched in large ion lithophile elements (LILEs) and depletion in high field strength elements (HFSEs), and show listric REE patterns. In-situ apatite Sr–Nd isotopes show limited variations (($^{87}Sr/^{86}Sr)_i$ = 0.7060–0.7068, ϵNd(t) = −4.8–0.2), which plot between Paleo-Tethys ocean-related arc magmas and the ancient crust in eastern Tibet. Zircon grains from this study and published studies have mostly positive yet variable ϵHf(t) values (−20.6 to +12.2) and young Hf model ages that overlap those of the Paleo-Tethys ocean-related arc magmas. The above Sr-Nd-Hf isotopes, together with the elevated zircon $\delta^{18}O$ values (6.4 to 9.3‰) and arc-like trace element patterns, collectively suggest that the Yulong intrusion may have originated from partial melting of juvenile lower arc crust related to the subduction of the Paleo-Tethys ocean, with incorporation of a small amount of ancient crustal materials.

Two generations of amphibole were recognized at Yulong. Their compositions are used to calculate crystallization depths, magmatic oxidation states, and water contents. The caculated results show that the early-stage euhedral high-Al (5.87–8.51 wt%) amphibole phenocrysts may have crystallized in the underlying magma chamber (7.1–12.5 km in depth), whereas the late-stage xenomorphic low-Al (3.47–4.87 wt%) amphibole grains may have crystallized in the porphyritic stock (4.0–5.6 km). Magmatic water contents decrease from early- (3.5–4.6 wt%) to late-stage (2.8–3.5 wt%) amphibole, which is interpreted to indicate fluid exsolution from the magma chamber during emplacement of the Yulong intrusion. Caculated oxidation states increase from early- (ΔNNO = 0.6–1.5) to late-stage (ΔNNO = 1.9–2.3) amphibole. Plagioclase phenocrysts show periodic or reverse core-to-rim zonation of An contents (range up to 25 mol%), which are coupled by FeO contents, probably suggesting magma recharge events. Collectively, we propose that the magma chamber beneath Yulong was recharged by a less evolved magma, and was saturated in fluids to produce intensive alteration and mineralization. The relatively high oxidation states allow the metals to be enriched in the evolving magma, and to be deposited in the hydrothermal alteration stage.

1. Introduction

Porphyry Cu deposits are typically developed in oceanic slab subduction-related magmatic arcs (Cooke et al., 2005; Sillitoe, 1972, 2010), and are genetically related to partial melting of the subduction-metasomatized asthenosphere mantle wedge (Richards, 2003, 2011). It is widely accepted that relatively high magmatic oxidation states (ΔFMQ > +1, where FMQ is the fayalite-magnetite-quartz buffer; Mungall, 2002; Ballard et al., 2002; Richards, 2015), high water contents (>4 wt%; Richards, 2011), and high sulfur and halogen contents (Streck and Dilles, 1998; Chelle-Michou and Chiaradia, 2017; Zhu et al., 2018; Xu et al., 2016b) are all indispensable conditions for porphyry Cu

* Corresponding author.
E-mail address: bixianwu@vip.gyig.ac.cn (X.-W. Bi).

mineralization. In addition, voluminous fluid exsolution and focused metal precipitation are also essential factors in producing high grade mineralization (Burnham, 1979; Candela, 1992; Richards, 2005).

Recent studies have shown that the postsubduction tectonic settings, such as the Miocene Gangdese belt and the Eocene Yulong belt in eastern Tethys domain, could also form porphyry Cu deposits (Hou et al., 2004, 2011, 2013; Richards, 2009; Shafiei et al., 2009; Li et al., 2011; Xu et al., 2012, 2016a; Deng et al., 2014, 2017). Origin of these ore-forming porphyries, however, remains a matter of debate. Several models have been proposed to account for the paragenesis of these postsubduction porphyry deposits, which include partial melting of the lithosphere mantle that was metasomatized by previous slab-derived melts/fluids (Zhang and Xie, 1997; Zhang et al., 1998; Gao et al., 2007, 2010; Xu et al., 2012, 2016a), partial melting of the subducted oceanic slab (Hu et al., 2015a), and partial melting of lower crustal cumulates of early arc magmas (juvenile lower arc crust) (Chung et al., 2003; Hou et al., 2004, 2006, 2011, 2013, 2015; Richards, 2009; Shafiei et al., 2009; Li et al., 2011; Wang et al., 2014, 2018).

The giant Yulong porphyry Cu–Mo deposit, located in eastern Tibet (Fig. 1A), is a typical postsubduction porphyry Cu–Mo deposit (Tang and Luo, 1995; Hou et al., 2003). Despite a mass of whole rock geochemical and zircon Hf isotopic studies, origin of the ore-related Yulong intrusion remains controversial. Major disputes include partial melting of the ancient subduction-metasomatized lithospheric mantle (Zhang and Xie, 1997; Zhang et al., 1998; Hou et al., 2003; Jiang et al., 2006), or the juvenile mafic arc lower crust (Hou et al., 2006; Li et al., 2012). In this contribution, we present new whole-rock major and trace element geochemistry, in-situ apatite Sr–Nd and zircon Hf–O isotopes of the ore-related Yulong intrusion, with the aim of providing new evidences for the origin of the postsubduction Yulong deposit. Textural and compositional features of silicate phenocrysts (amphibole and plagioclase) of the Yulong intrusion are also reported to shed lights the variations of magmatic oxygen fugacity and water contents during magmatic-hydrothermal evolution, which finally led to the porphyry Cu mineralization.

2. Geological setting

2.1. Geology of the Yulong porphyry Cu belt

The 30-km-wide and >300-km-long Yulong porphyry Cu belt is situated in the north Qiangtang terrane in eastern Tibet (Fig. 1A–B; Hou and Zhang, 2015). The north Qiangtang terrane consists of Proterozoic to early Paleozoic basement and middle Paleozoic–Mesozoic carbonate and clastic cover rocks (Tang and Luo, 1995). It is separated from the Songpan-Ganze terrane by the Permian Jiangda-Weixi arc, which is product of the subduction of the Jinshajiang Ocean (a branch of the Paleo-Tethys ocean) during Permian-Triassic (Fig. 1B; Hou et al., 2003; Zi et al., 2012a). To the west, the north Qiangtang terrane is separated from south Qiangtang terrane by the Permian-Triassic Zuogong-Jinghong arc (Fig. 1B). This arc marks the closure of Longmu Tso–Shuanghu Ocean in Triassic, which is considered to have been the main branch of the Paleo-Tethys Ocean in eastern Tibet (Fig. 1B; Li et al., 2007).

The NW–SE-trending Yulong belt hosts one giant (Yulong, 6.5 Mt Cu and 0.41 Mt Mo; Tibet Yulong Copper Co. Ltd., 2009), three large (Malasongduo, 1 Mt Cu, 37.1 Ma; Duoxiasongduo, 0.5 Mt Cu, 37.2 Ma; Narigongma, 0.5 Mt Cu, 43.6–41.7 Ma; Liang et al., 2006; Hou et al., 2003; Yang et al., 2014a), and three medium to small (Baomai, 0.21 Mt Cu; 42.7 Ma; Zhanaga, 0.30 Mt Cu, 38.5 Ma; Mangzong, 0.25 Mt Cu, 37.5 Ma; Lin et al., 2018; Liang et al., 2006) porphyry Cu deposits. Formation and distribution of these deposits are structurally controlled by the crustal scale strike-slip faults that were resulted from the Cenozoic India-Asian continental collision (Fig. 1B; Hou et al., 2003). Because the subduction of the Jinshajiang
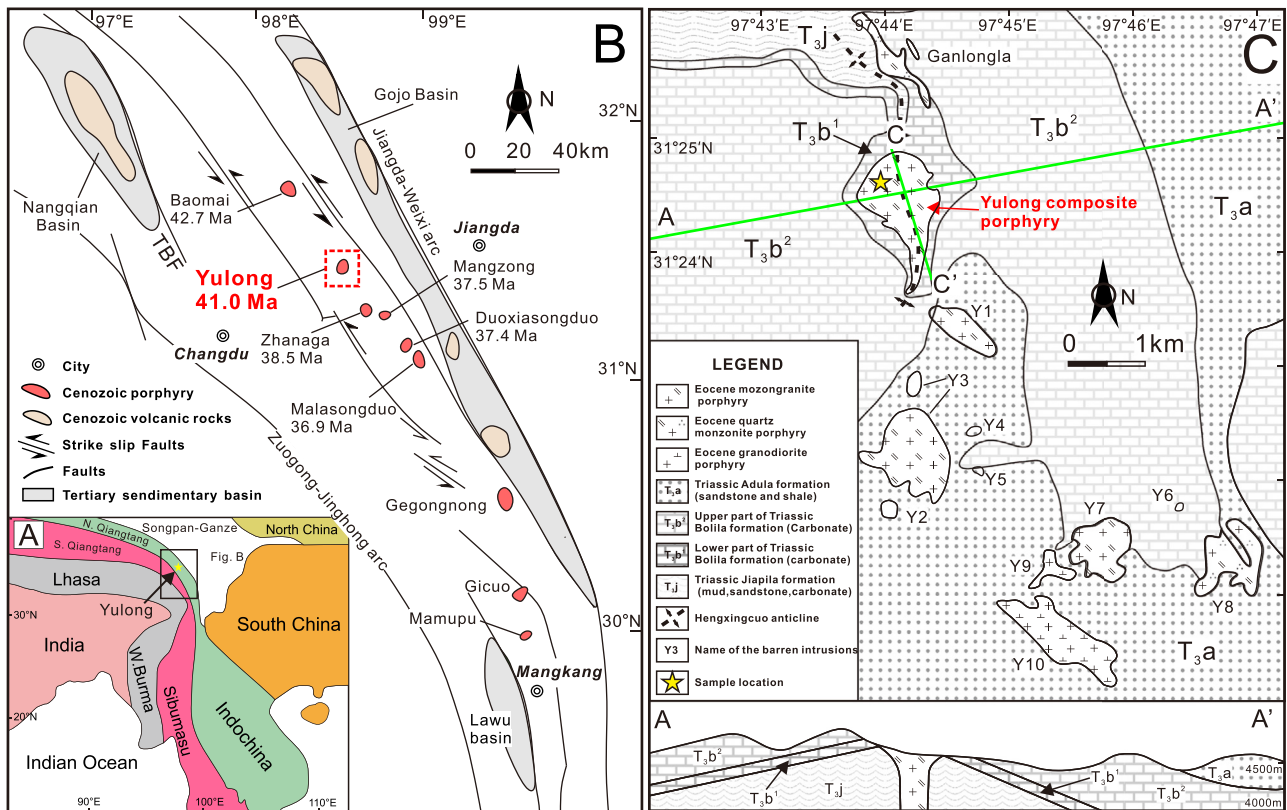

Fig. 1. A. Simplified geological map of southeastern Tibet (Modified from Metcalfe, 2013). B. Simplified geological map of the Yulong porphyry Cu belt in eastern Tibet, showing distribution and ages of Cenozoic porphyry Cu deposits (Modified from Hou et al., 2003). The ages of the deposits are from Liang et al. (2006), Li et al. (2012) and Lin et al. (2018). C. Simplified geological map of the Yulong ore district (Modified from exploration report of the Tibet Yulong Copper Co., Ltd., 2009).

and Longmu Tso—Shuanghu Ocean both have been completed before late Triassic (Li et al., 2007; Zhu et al., 2011; Zi et al., 2012a; He et al., 2018; Yang et al., 2018) in this region, and the Neo-Tethys ocean had also closed before 65—55 Ma (Mo et al., 2007; Hu et al., 2015b), these Eocene porphyry deposits (~42 Ma) apparently belong to postsubduction porphyry deposits (Richards, 2009).

2.2. Deposit geology

As the largest deposit in the Yulong belt, the Yulong porphyry Cu—Mo deposit is spatially and genetically related to the Yulong composite porphyry stock (Fig. 1C), which intruded the Triassic sandstone, mudstone and limestone. These sedimentary rocks may also have contributed some of the ore-forming materials (e.g., Pb; Huang et al., 2019a). The Yulong composite porphyry stock consists of three magmatic phases: early stage monzongranite porphyry (MGP), middle stage K-feldspar porphyry (KGP), and late stage quartz albite porphyry (QAP) (Fig. 2; Chang et al., 2017). Copper and Mo mineralization is mainly related to and hosted by the early stage MGP, which contains phenocrysts of quartz, plagioclase, K-feldspar, biotite and amphibole (Fig. 3A-D). Age of the MGP has been dated to be 40.9 ± 0.2 Ma to 41.3 ± 0.8 Ma (zircon U—Pb, 2σ; Guo et al., 2006; Liang et al., 2006; Wang et al., 2009; Li et al., 2012; Huang et al., 2019b), with an slightly older age reported to be 42.0 ± 0.3 Ma (Chang et al., 2017). The middle stage KGP occurs as small dikes, and yields zircon U—Pb ages of 41.2 ± 0.3 Ma, which is indistinguishable from the MGP (2σ; Chang et al., 2017). Small portion of Cu or Mo mineralization (<20%) was produced by this phase (Chang et al., 2017). The late stage quartz albite porphyry (QAP; Fig. 2) postdates the Cu and Mo mineralization (Chang et al., 2017), and yields zircon U—Pb age of 40.1 ± 0.3 Ma (2σ;

Chang et al., 2017). The QAP also occurs as small dikes. No economic Cu or Mo mineralization was produced by this phase.

The bulk Yulong composite porphyry stock had experienced intense to moderate potassic alteration, which is mainly associated with the former two magmatic phases (MGP and KGP; Fig. 2; Chang et al., 2017). The potassic alteration is expressed by various types of A veins such as biotite veins (Fig. 3E) and quartz + chalcopyrite + molybdenite veins (Fig. 3A; Chang et al., 2017), and by the replacement of amphibole phenocrysts by secondary biotite (Fig. 3F). Deposition of Cu and Mo mainly occurred in this stage (Fig. 2; Chang et al., 2017, 2018). Phyllic alteration is locally developed along with the occurrence of QAP, and commonly overprints the precursory potassic alteration (Fig. 2). Intensive argillic alteration developed in the upper part of the Yulong intrusion, and at the contacts between the intrusion and wall rocks (Fig. 2). No economic Cu or Mo mineralization was produced in the phyllic and argillic alteration stages (Chang et al., 2017).

Apart from the mineralized Yulong composite porphyry stock, the Yulong ore district also hosts several coeval subeconomic intrusions (Fig. 1B; the Ganlongla intrusion, 43.9 ± 0.6 Ma to 43.6 ± 0.8 Ma, Guo et al., 2006; Wang et al., 2009; the Y3 intrusion, 41.4 ± 0.6 Ma; Wang et al., 2011). The subeconomic intrusions have indistinguishable whole rock major and trace element compositions, whole-rock Sr—Nd and in-situ zircon Hf isotopes with the mineralized MGP of the Yulong composite porphyry stock (Jiang et al., 2006; Wang et al., 2011; Li et al., 2012), indicating that they are co-magmatic (Zhang and Xie, 1997; Hou et al., 2003; Jiang et al., 2006; Xu et al., 2012, 2016a; Hou et al., 2011; Li et al., 2012). Previous study have shown that all these intrusions were relatively oxidized, hydrous, and sulfur-rich, and were fertile for ore-
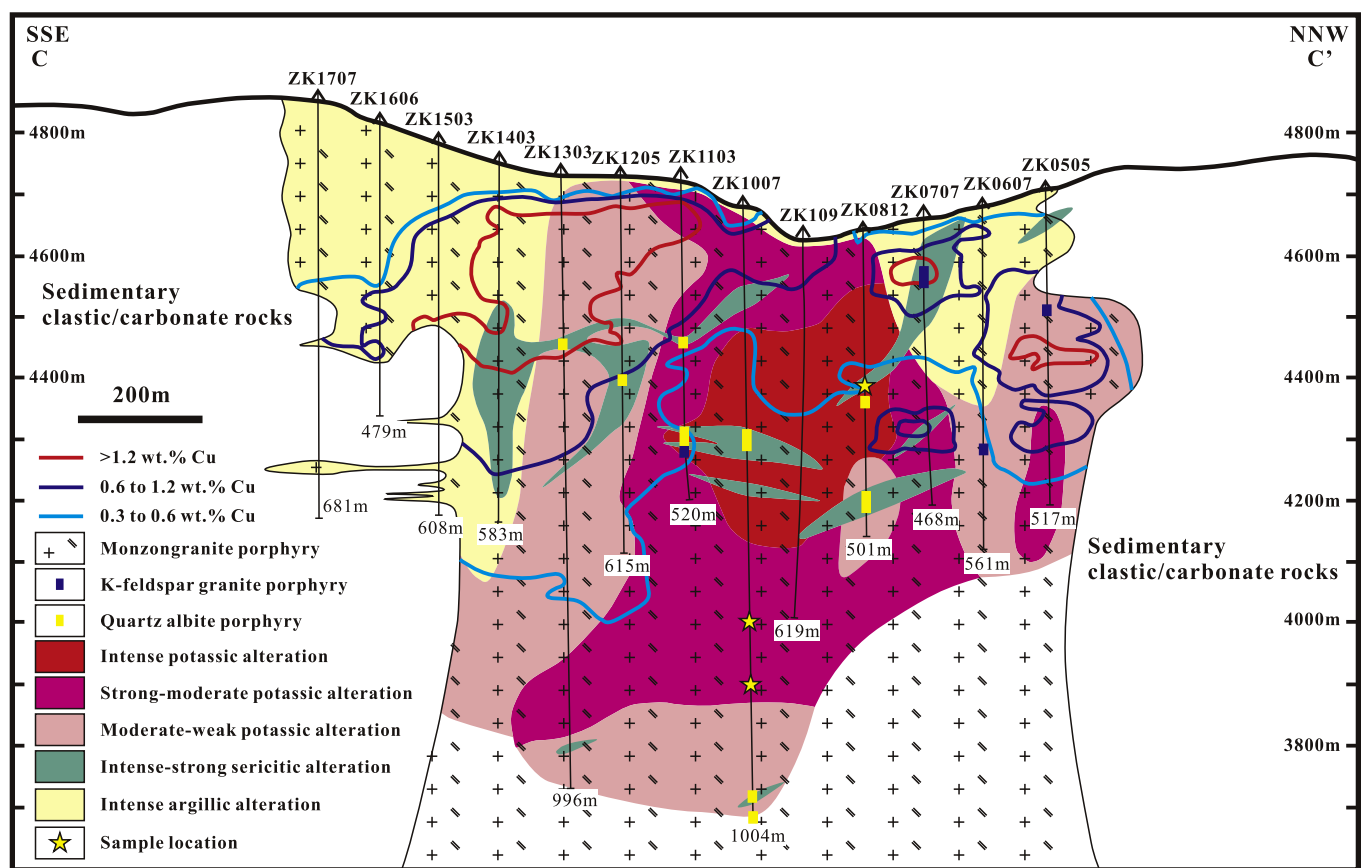

Fig. 2. Geological cross-section C-C′ of the mineralized Yulong intrusion, showing variation of ore grades, hydrothermal alteration, and occurrence of different magmatic phases (After Chang et al., 2017). The middle-stage K-feldspar granite porphyry and late-stage quartz albite porphyry occur as small dikes that intrude the early-stage monzogranite porphyry. Location of cross-section C-C′ is shown in Fig. 1B.
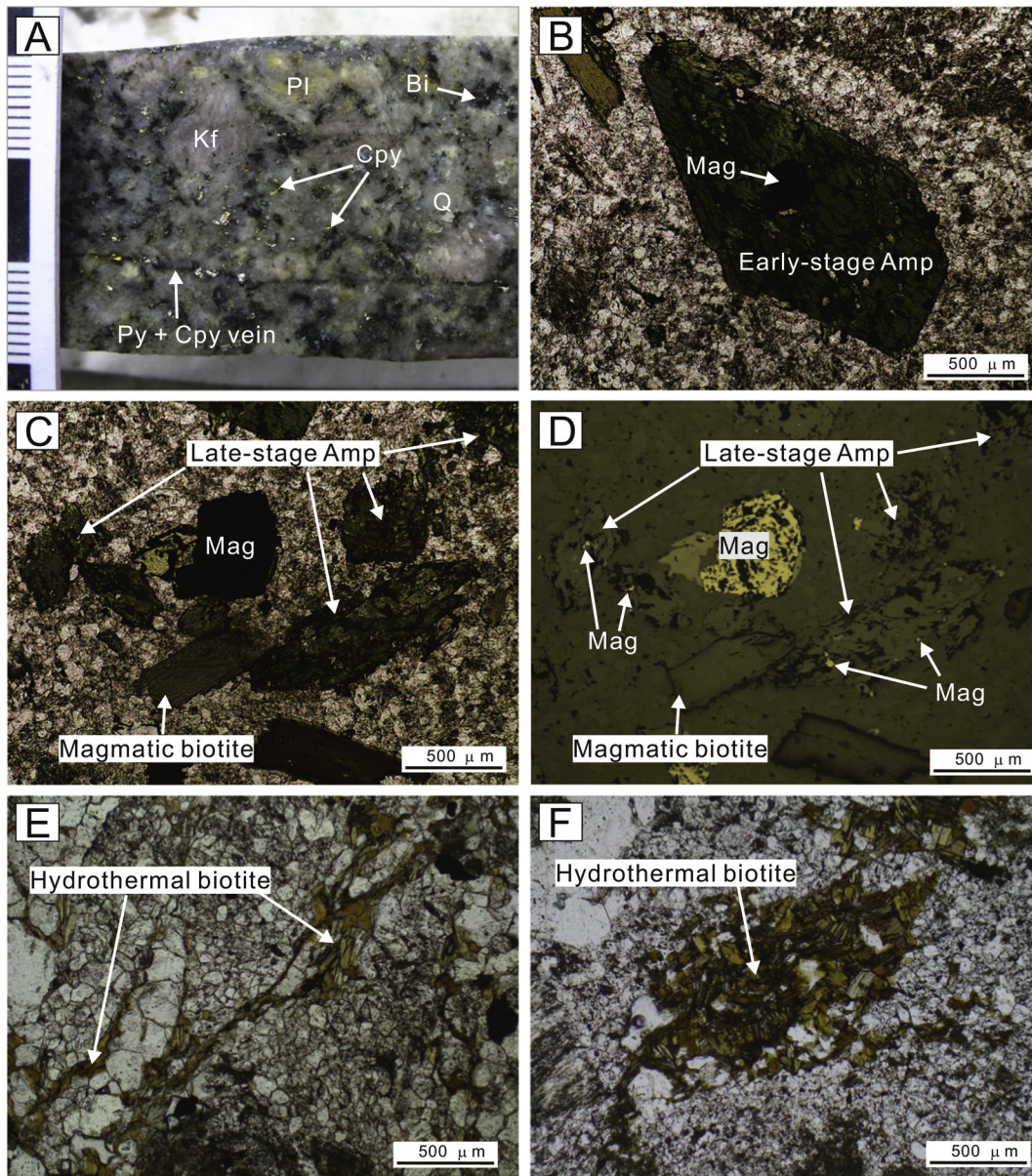
Fig. 3. Representative photographs and microphotographs of porphyry-type ores from the Yulong deposit. A. Porphyry ores with disseminated chalcopyrite and pyrite, and pyrite + chalcopyrite veins. B. Transmitted light microphotographs showing the euhedral early-stage high-Al amphiboles from the Yulong deposit. C. Transmitted light microphotographs showing the late-stage low-Al amphiboles. They are mainly developed in the groundmass, and are subhedral to xenomorphic in shape and smaller in size. D. Reflected light microphotographs of (C), showing that the late-stage low-Al amphiboles coexist with magnetite. E. Hydrothermal biotite veins formed in potassic alteration stage. F. Hydrothermal biotite formed by alteration of amphibole phenocrysts. Abbreviations: Amp = amphibole, Bi = biotite, Cpy = chalcopyrite, Kf = K-feldspar, Mag = magnetite, Moly = molybdenite, Pl = plagioclase, Py = pyrite, Q = quartz, Ttn = titanite.

formation, whereas the mineralized Yulong composite porphyry stock was more extensively devolatilized, which was possibly triggered by magmatic recharge events (Huang et al., 2019b).

3. Sampling and analytical methods

Drill core samples from the *syn*-mineralization MGP were collected and petrographically studied to seek least-altered phenocrysts (plagioclase and amphibole) for electron microprobe analysis, and the apatite crystals for in-situ Sr–Nd isotope analyses. Locations of the collected samples are shown in Figs. 1C and 2, and are described in Appendix Tables A1–A5. Twelve least-altered samples (MGP) were collected at the open pit for whole-rock major and trace element analysis. For convenience, the MGP is referred to as the Yulong intrusion in the following text.

Four samples from the mineralized Yulong intrusion (MGP; YL912, YL906, ZK0812-389, ZK1007-607) were used for in-situ zircon Hf–O isotope analysis. Three of these samples have been previously dated to be 43.2 ± 0.3 Ma (YL912, Xu et al., 2012), 41.1 ± 0.3 Ma (sample ZK0812–389), and 40.9 ± 0.3 Ma (sample ZK1007–607), respectively (zircon U–Pb, 2σ; Huang et al., 2019b).

3.1. Electron microprobe analyses

Compositional data of plagioclase and amphibole were acquired by a JEOL JXA-8230 electron microscope using wavelength-dispersive spectroscopy at the Shandong Bureau Testing Center of China Metallurgical Geology Bureau (Jinan). The operating conditions are 15 kV accelerating voltage, 10 nA beam current, and 5 μm beam diameter. All data were corrected based on the ZAF
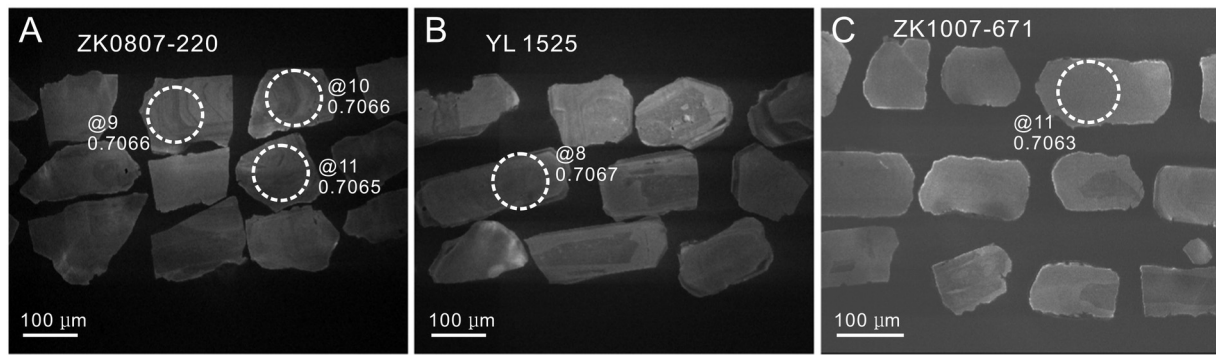
Fig. 4. Representative CL images of the apatite crystals used for in-situ Sr–Nd isotope analyses. Also shown are the analytical spots and representative analytical results of Sr isotopes.

procedure. The following standards were used for element calibrating: phlogopite (F), jadeite (Na and Si), diopside (Ca, Mg), garnet (Al), olivine (Fe), rhodonite (Mn), apatite (P), barite (Ba), rutile (Ti) and sanidine (K). The peak/background counting times were 8 s/3 s for Na, 10s/5s for Mg, Al, Si, Ni, K, Ti, Ca, P, F and Cl, and 20s/10s for Mn, Fe and Cr.

3.2. Whole-rock major and trace element analyses

Whole-rock major element compositions were determined using an Axios PW4400 X-ray fluorescence spectrometer (XRF) at ALS Chemex, Guangzhou, China, using fused lithum-tetraborate glass pellets. The analytical accuracy is better than 5 relative %. Whole

Table 1
Whole-rock major (%) and trace (ppm) element compositions of the Yulong intrusion.

Sample	YL1522	YL1523	YL1524	YL1525	YL1525-4	YL1525-7	YL1528-2-1	YL1528-2-2	YL1530	YL1549-2	YL1552-26	YL1552-3
SiO_2	69.3	69.5	68.6	66.5	66.3	67.4	68.8	67.5	66.9	67.6	68.2	68.3
TiO_2	0.37	0.34	0.37	0.38	0.36	0.38	0.36	0.35	0.37	0.35	0.36	0.37
Al_2O_3	15.3	14.9	15.2	15.1	15.0	15.5	15.3	14.9	15.2	15.1	15.4	15.5
TFe_2O_3	2.21	2.46	3.18	3.85	3.08	3.31	2.44	3.22	2.99	2.75	2.05	2.39
MnO	0.01	0.02	0.01	0.01	0.01	0.01	0.02	0.01	<0.01	<0.01	0.01	0.01
BaO	0.15	0.11	0.11	0.09	0.12	0.13	0.11	*	0.12	0.15	0.15	0.14
MgO	0.93	1.06	1.13	1.18	1.06	1.22	1.04	1.13	1.24	1.12	0.63	0.76
CaO	1.22	1.72	1.52	1.08	1.50	1.08	2.07	1.08	1.32	1.44	2.4	2.44
Na_2O	3.06	3.44	3.61	3.22	3.79	3.88	3.72	3.96	3.18	3.40	3.51	3.50
K_2O	4.98	4.68	4.40	5.34	4.54	4.53	4.44	4.33	5.10	5.26	5.16	4.95
P_2O_5	0.18	0.19	0.21	0.21	0.20	0.22	0.20	0.20	0.22	0.20	0.21	0.21
LOI	1.17	1.23	1.39	2.38	1.85	2.34	1.06	2.36	1.93	1.88	1.20	1.27
SUM	98.7	99.5	99.6	99.3	97.7	99.9	99.5	99.0	98.5	99.1	99.1	99.6
Mg#	46	46	42	38	41	42	46	41	45	45	38	39
La	55.6	82.1	71.9	71.1	72.9	62.1	67.8	71.9	63.7	68.0	48.4	43.3
Ce	105	158	141	141	141	120	130	137	115	131	123	104
Pr	10.8	16.1	14.8	14.9	15.1	12.7	13.5	13.9	11.6	13.3	14.1	12.0
Nd	36.9	56.0	52.1	51.2	53.8	44.7	47.4	49.2	39.3	46.6	52.4	44.7
Sm	6.04	8.71	8.39	8.65	8.70	7.19	7.49	7.77	6.06	7.18	8.73	7.62
Eu	1.82	2.14	2.13	2.28	2.42	1.70	1.91	1.86	1.77	1.76	2.25	1.94
Gd	4.06	5.52	5.43	5.48	6.10	5.04	4.94	5.12	4.40	4.58	5.69	5.06
Tb	0.53	0.66	0.67	0.67	0.76	0.64	0.60	0.64	0.56	0.56	0.67	0.61
Dy	2.66	3.24	3.16	3.25	3.68	3.21	3.06	3.09	2.84	2.62	3.17	2.85
Ho	0.53	0.58	0.59	0.55	0.63	0.61	0.53	0.55	0.53	0.47	0.53	0.53
Er	1.44	1.57	1.59	1.53	1.68	1.61	1.50	1.51	1.51	1.26	1.49	1.42
Tm	0.22	0.21	0.22	0.22	0.23	0.22	0.20	0.20	0.22	0.17	0.21	0.19
Yb	1.31	1.26	1.31	1.27	1.37	1.28	1.28	1.26	1.25	1.00	1.17	1.19
Lu	0.21	0.19	0.21	0.21	0.19	0.20	0.19	0.20	0.19	0.16	0.18	0.18
Hf	7.50	6.50	6.80	6.60	6.00	6.50	7.50	6.10	5.70	5.50	5.60	6.70
Y	13.6	15.6	15.7	16.6	17.4	16.2	15.2	15.7	15.5	13.5	15.1	15.6
Rb	239	189.5	207	276	195.0	196.0	218	201	254	240	237	231
Sr	780	963	998	764	1020	896	1065	831	871	1030	1100	1075
Nb	11.7	10.7	11.4	11.1	10.5	11.0	11.8	11.5	10.2	11.4	10.9	11.3
Ta	1.50	1.20	1.30	1.40	1.30	1.20	1.40	1.20	1.30	1.30	1.20	1.30
Th	26.3	23.3	23.5	23.2	23.2	22.0	26.9	25.9	22.1	23.1	26.0	17.90
U	10.7	4.78	7.25	4.73	10.1	6.72	9.24	14.6	7.99	9.46	4.75	4.90
V	56	52	58	65	55	54	56	53	57	55	51	53
W	681	499	630	942	737	604	734	704	735	830	563	747
Zr	271	242	255	245	217	241	278	219	220	206	202	254
Ba	1240	914	941	830	1105	1195	965	1025	1075	1315	1250	1170
Cr	20	14	17	14	14	14	13	13	13	13	11	12
Ni	20.4	15.7	19.1	19.6	19.5	17.1	18.1	20.8	20.7	21.0	12.4	17.5
Cs	11.65	5.39	5.82	9.67	6.90	9.61	13.50	9.97	10.50	7.06	6.65	7.31
Ga	20.8	21.2	23.2	18.1	21.1	21.9	23.1	22.3	21.5	20.8	20.8	20.9
Cu	672	269	1450	666	2580	557	609	1180	5190	980	2060	1210
Li	20.6	21.1	22.7	28.5	17.5	21.2	19.9	20.0	22.1	19.2	10.6	11.0
Mo	6.14	8.95	3.26	6.08	2.58	1.62	2.36	2.18	5.62	6.04	166.5	26.9
La/Yb	42.4	65.2	54.9	56.0	53.2	48.5	53.0	57.1	51.0	68.0	41.4	36.4

rock trace elements were determined using a PerkinElmer DRC-e ICP-MS at IGCAS. About 50 mg powdered samples were precisely weighted and dissolved in high-pressure Teflon bombs with HF and HNO_3 mixture for 2 days at 190 °C. To monitor signal drift during counting, Rh was used as an internal standard. Detailed analytical methods were given by Qi et al. (2000). The analytical precision is generally better than 10%.

3.3. Apatite Sr and Nd isotope analyses

Apatite is a ubiquitous accessory mineral in granitic rocks, and is relatively insensitive to later hydrothermal alteration (e.g., Mao et al., 2016). It could preserve the original chemical and isotopic features of the parental magmas (Poitrasson et al., 2002). Considering the fact that whole-rock samples at Yulong have been subjected to varying degrees of hydrothermal alteration, we therefore chose apatite for Sr–Nd isotope analyses. The apatite grains analyzed in this study are generally rectangular in shape, and show oscillatory zonings in cathodoluminescence (CL) images, suggesting a magmatic origin (Fig. 4A–C).

In-situ apatite Sr and Nd isotopic compositions were analyzed by laser ablation that is coupled to a Neptune multi-collector ICP-MS (LA-MC-ICP-MS) at the institute of geology and geophysics, Chinese Academy of Sciences (IGGCAS). The analytical protocol follows the method described in Yang et al. (2009, 2014b). For Sr isotope analyses, the repetition rate was 8 Hz and spot size was 120 μm. Apatite reference materials AP1 and Slyudyanka were used as quality control materials. They yielded average $^{87}Sr/^{86}Sr$ values of 0.71136 ± 14 (2SD, $n = 22$) and 0.70766 ± 12 (2SD, $n = 28$), respectively, which are in agreement with the recommended values (0.711370 ± 31 and

0.70769 ± 15, respectively; Yang et al., 2014). For Nd isotope analyses, the repetition rate was 8 Hz and spot size was 90 μm. Apatite reference materials AP1 and AP2 were used as external standards. They yielded average $^{143}Nd/^{144}Nd$ values of 0.511345 ± 38 (2SD, $n = 18$) and 0.511011 ± 40 (2SD, $n = 21$), respectively, which are in agreement with the recommended values (0.511349 ± 38 and 0.511007 ± 30, respectively, 2SD; Yang et al., 2014b). The following values are used to calculate the initial Sr (($^{87}Sr/^{86}Sr)_i$) and Nd ($\epsilon Nd(t)$) isotopic compositions: age = 41 Ma (Liang et al., 2006; Li et al., 2012); $\lambda_{Rb} = 1.42 \times 10^{-11}$ year^{-1}(Steiger and Jäger, 1977); $\lambda_{Sm} = 6.54 \times 10^{-12}$ year^{-1} (Lugmair and Marti, 1978); $(^{143}Nd/^{144}Nd)_{CHUR} = 0.512638$ (Goldstein et al., 1984); $(^{147}Sm/^{144}Nd)_{CHUR} = 0.1967$ (Jacobsen and Wasserburg, 1980).

3.4. Zircon O and Hf isotope analyses

In-situ zircon O isotope analyses of samples YL912 and YL906 were conducted at the Institute of Geology and Geophysics (IGG), Chinese Academy of Sciences (CAS) in Beijing, using a Cameca IMS 1280 ion probe. Detailed analytical procedures were similar to those described by Li et al. (2009). The Cs^+ primary ion beam was used as the ion source. Spot size of about 20 μm was applied. One analysis takes about 5 min. Uncertainties on individual analysis are usually better than 0.2‰-0.3‰ (1σ; Li et al., 2009, 2010). The instrumental mass fractionation factor (IMF) is corrected using zircon 91,500 standard with a $\delta^{18}O$ value of 9.9‰ (Wiedenbeck et al., 2004; Li et al., 2009). Zircon O isotopes of samples ZK1812-389 and ZK1007-607 were determined using Cameca IMS-1280 SIMS at Guangzhou Institute of Geochemistry (GIG), CAS. Analytical procedures were similar to those described above. The spot sites of
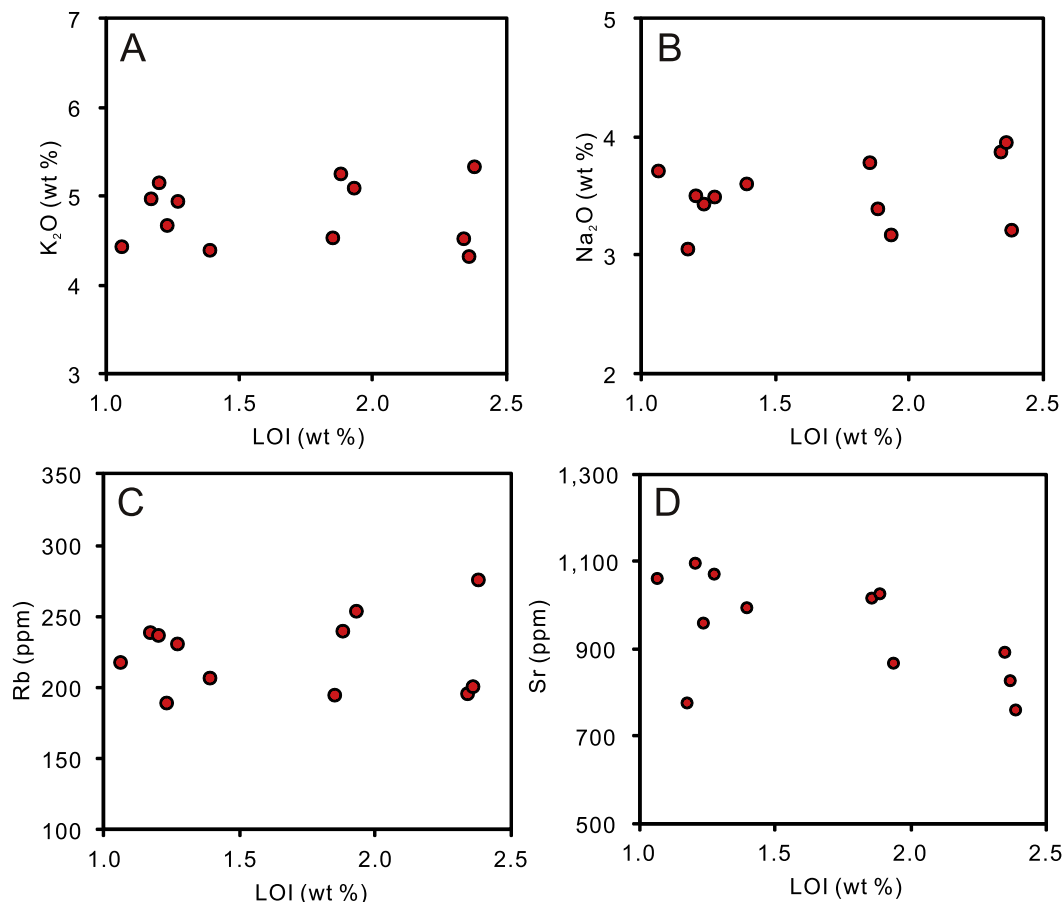

Fig. 5. Plots of fluid-mobile elements (K, Na, Rb and Sr) versus LOI values of the Yulong intrusion.

in-situ zircon O isotope analyses were selected to be next to the sites of previous U–Pb isotope analyses. Instrumental mass fractionation factor during analysis is corrected using the Penglai and Qinghu zircon standards that yield $\delta^{18}O$ values of 5.31‰ ± 0.10‰ (2SD) and 5.4‰ ± 0.2‰ (2SD), respectively (Li et al., 2010, 2013).

In-situ zircon Hf isotope analyses of samples YL912 and YL906 were conducted at IGGCAS, using a Neptune multi-collector ICP-MS equipped with a Geolas 193 nm laser-ablation system. The spots of Hf isotope analyses were selected to be next to the spots of O analyses. Detailed analytical methods were described by Wu et al. (2006). Zircon 91,500 was used as external standard. Our determined $^{176}Hf/^{177}Hf$ ratios of zircon standards 91,500 (0.282308 ± 0.000011) are well consistent with reported values (0.282306 ± 0.000028; Woodhead et al., 2004).

4. Results

4.1. Whole-rock major and trace element compositions

Whole-rock major and trace element compositions of the Yulong intrusion are listed in Table 1, and illustrated in Figs. 5–7.

The Yulong intrusion has been subjected to varying degrees of hydrothermal alteration (Figs. 2 and 3A–F), which may affect the whole-rock compositions, especially these of the fluid-mobile elements such as K, Na, Rb, and Sr. To evaluate the potential effects of alteration on whole-rock compositions, the contents of these mobile elements (e.g., K, Na, Rb and Sr) are plotted versus loss-on-ignition (LOI) values (Fig. 5). These plots show relatively constant contents for the mobile elements with varying LOI values, suggesting that alteration may only have minimal effect on the compositions of the studies samples.

The samples are compositionally homogenous, characterized by high SiO_2 (66.3–69.5 wt%), Al_2O_3 (14.9–15.5 wt%), K_2O (4.33–5.34 wt %) contents, and low MgO (0.63–1.24%) and Cr (<30 ppm) contents and $Mg^{\#}$ values (Table 1; Fig. 6A–D). Major element compositions of these samples were normalized to LOI free before geochemical plotting. In the $Zr/TiO_2 * 0.0001$ versus Nb/Y diagram, these samples mostly straddle the boundaries between rhyolite/granite, trachyandesite/syenite, and rhyodacite/granodiorite fields (Fig. 6A). In primitive mantle-normalized extended trace element diagram (Fig. 7A), these samples are characterized by enrichment in large ion lithophile elements (LILEs, Rb, Ba, Th, U and K) and depletion in high field strength elements (HFSEs, Nb, Ta, Ti and P), similar to typical subduction-related igneous rocks (Hawkesworth et al., 1993; Pearce, 1996). In the chondrite-normalized rare earth element (REE) diagram (Fig. 7B), these rocks are characterized by right inclined, listric-shaped patterns, likely suggesting amphibole fractionation during evolution of the hydrous magma (Castillo et al., 1999; Richards and Kerrich, 2007). These samples also have high La/Yb (36.4–68.0) and Sr/Y (46.0–76.3) ratios, and plot in the adakite field in the La/Yb versus Yb diagram (Fig. 7C–D).

4.2. Apatite Sr and Nd isotopes

The analytical results of apatite Sr and Nd isotopes are listed in Appendix Tables A1 and A2, respectively. Apatite grains from the Yulong intrusion have very low $^{87}Rb/^{86}Sr$ ratios ranging from 0.0003 to 0.0146, suggesting negligible radiogenic ^{87}Sr contribution after apatite formation. They have very uniform $^{87}Sr/^{86}Sr$ ratios ranging from 0.7060 to 0.7068, corresponding to initial Sr isotopic values (i.e. $(^{87}Sr/^{86}Sr)_i$) of 0.7060 to 0.7068 at 41 Ma (age of the ore-related Yulong intrusion; Liang et al., 2006; Li et al., 2012). These values conform to a Gaussian distribution, with the peak values at 0.7064 to 0.7066 (Fig. 8A). The apatite grains have $^{147}Sm/^{144}Nd$ and
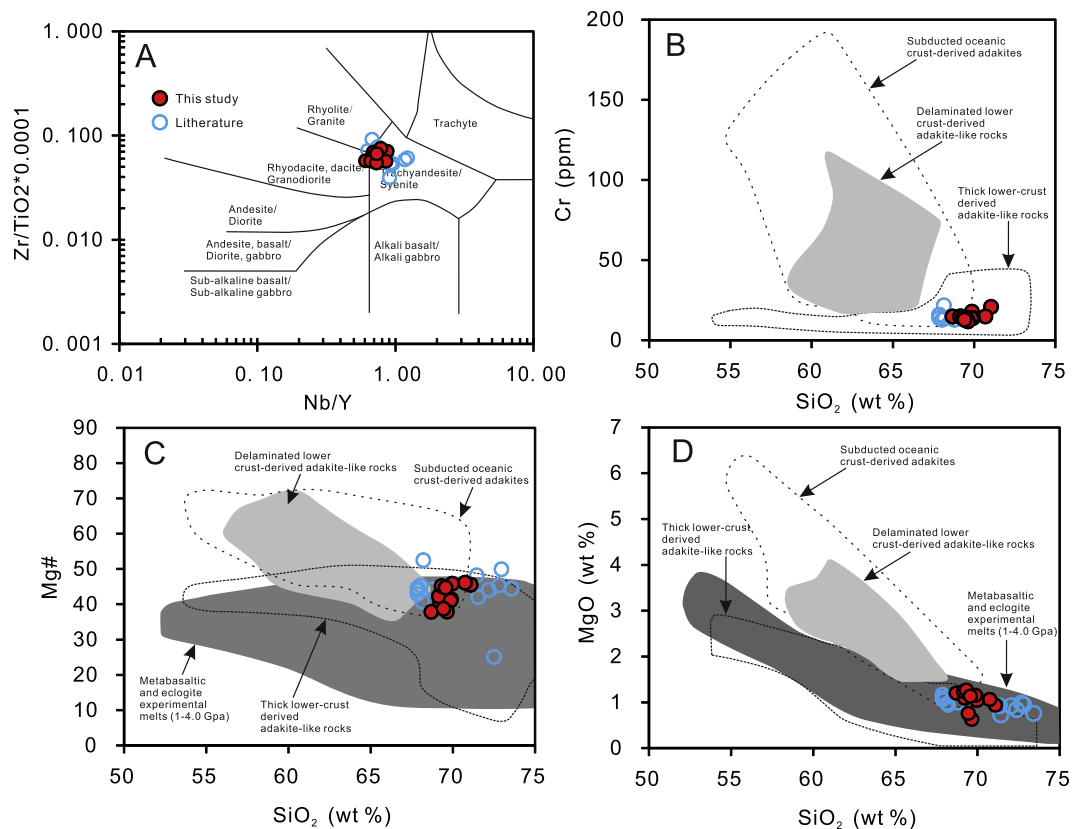

Fig. 6. (A) $Zr/TiO_2*0.0001$ vs. Nb/Y discrimination diagram (Winchester and Floyd, 1977), (B) Cr (ppm) vs SiO_2 (wt%) diagram, (C) $Mg^{\#}$ vs SiO_2 (wt%) diagram, and (D) MgO (wt%) vs. SiO_2 (wt%) diagram for the Yulong intrusion. Data from published studies (Jiang et al., 2006; Huang et al., 2019b) are also plotted. Reference fields in B-D are from Wang et al. (2006).
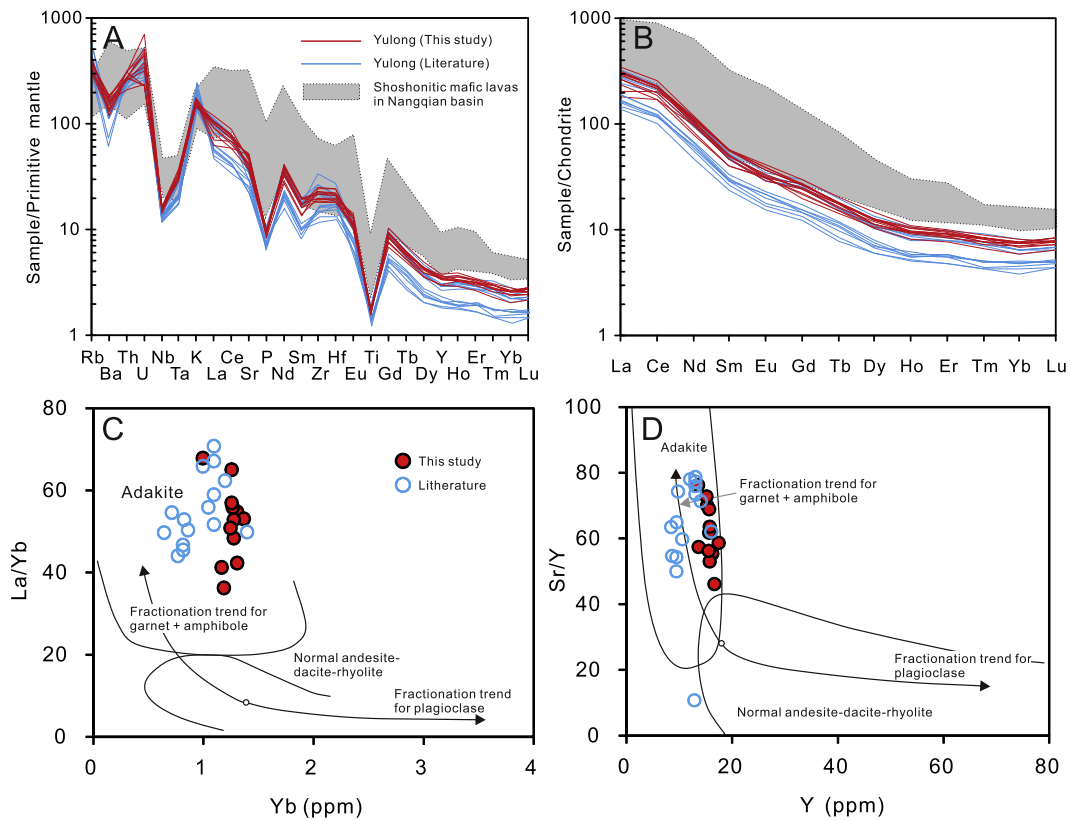
Fig. 7. (A) Primitive mantle-normalized trace element spider diagram, (B) Chondrite-normalized rare earth element patterns, (C) La/Yb vs. Yb diagram, and (D) Sr/Y vs. Y diagram for the Yulong intrusion. Normalization values of primitive mantle and chondrite are from Sun and McDonough (1989). Fields for mafic lavas in the Nangqian basin in A-B are from Deng et al. (2001) and Spurlin et al. (2005). Fields for adakite and normal andesite-dacite-rhyolite, and trends for mineral fractionation in C-D are from Richards and Kerrich (2007). Data sources of Yulong are the same as those in Fig. 6.

$^{143}Nd/^{144}Nd$ ratios ranging from 0.0731 to 0.1524 and from 0.51238 to 0.51262, respectively. Corresponding initial Nd isotopic values (i.e. $\epsilon Nd(t)$) range from −4.8 to +0.2. They also conform to a Gaussian distribution, with the peak values at −3 to −2 (Fig. 8B).

Initial Sr and Nd isotope compositions of the samples used for in-situ apatite Sr and Nd isotope analysis are caculated based on average values of all the apatite analyses in the corresponding sample. The results are summarized in Table 2 and illustrated in Fig. 9B. Published whole-rock Sr and Nd isotopes of the Yulong intrusion are also compiled and illustrated in Figs. 8A−B and 9B. Caculated initial Sr and Nd isotope compositions show limited variations, with the $(^{87}Sr/^{86}Sr)_i$ values ranging from 0.7062 to 0.7066, and $\epsilon Nd(t)$ ranging from −3.0 to −1.7.

4.3. In-situ zircon Hf−O isotopes

The analytical results of zircon Hf−O isotopes of samples YL906 and YL912 are listed in Table 3, whereas the zircon O isotopes of samples ZK0812-389 and ZK1007-607 are listed in Appendix Table A3. All data are illustrated in Figs. 8C−D, 9A, and 10. The $\epsilon Hf(t)$ values and two-stage model ages (T_{DM2}) were caculated back to 41 Ma (age of the Yulong intrusion; Liang et al., 2006; Li et al., 2012; Huang et al., 2019b). For comparison, published zircon Hf isotopes of the Yulong intrusion (Jiang et al., 2006; Wang et al., 2011; Li et al., 2012) are also compiled and illustrated in Figs. 8C and 10.

Zircon grains from samples YL906 and YL912 in this study have positive $\epsilon Hf(t)$ values ranging from 0.6‰ to 4.8‰ (average = 2.4 ± 1.1‰, n = 41), with model ages ranging from 811 to 1080 Ma (Fig. 10; Table 3). The $\epsilon Hf(t)$ values of this study and published studies conform to a Gaussian distribution, with the peak values at 0‰ to 5‰ (Fig. 8C). Several analyses from published study

(Jiang et al., 2006; Li et al., 2012) yielded significantly negative zircon $\epsilon Hf(t)$ values (Figs. 8C and 10), possibly implying involvement of crustal components during the formation of Yulong intrusion.

Oxygen isotopes of zircon grains from the Yulong intrusion show large variations from 6.4 to 9.3‰ (Figs. 8D and 9A; n = 79). These data conform to a Gaussian distribution, with the peak values at 6.8‰ to 7.2‰ (Fig. 8D). Most of the zircon $\delta^{18}O$ values range from 6.4 to 7.6‰ (average = 7.0 ± 0.3‰, 2σ, n = 74; Table 3; Appendix Table A3). A few zircons have higher $\delta^{18}O$ values ranging from 7.9 to 9.3‰ (Table 3; Appendix Table A3; Figs. 8D and 9A), possibly implying involvement of supracrustal components during the formation of Yulong intrusion.

4.4. Mineral compositions

Compositions of amphibole and plagioclase phenocrysts are listed in Appendix Tables A4 and A5, respectively.

4.4.1. Amphibole compositions

Two generations of amphibole were recognized in the Yulong intrusion. The early-stage amphibole grains occur as euhedral phenocrysts, which commonly enclose mineral inclusions such as apatite and magnetite (Fig. 3B). They have relatively high Al_2O_3, FeO, TiO_2, and Na_2O contents, and lower SiO_2, MgO, and CaO contents ($Al_2O_3 = 5.87−8.51$ wt%; $SiO_2 = 44.70−48.66$ wt%; Appendix Table A4; Fig. 11A−F), and are mainly classified as magnesio-hastingsite (Fig. 12A; Hawthorne et al., 2012). In comparison, the late-stage amphibole grains were developed in the groundmass, and are subhedral to xenomorphic in shape and smaller in size (Fig. 3C). They also enclose magnetite mineral inclusions (Fig. 3D), indicating
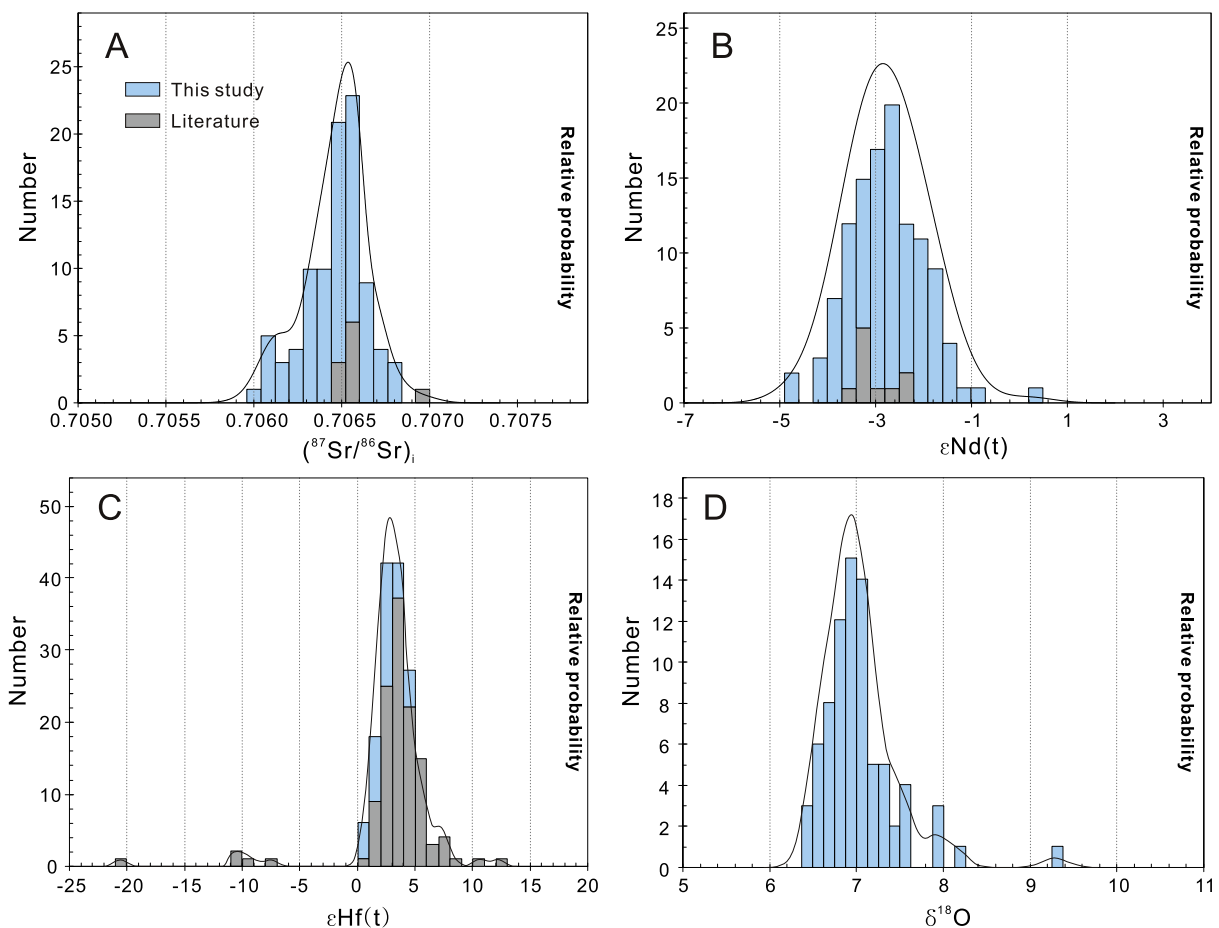
Fig. 8. Histograms and relative probability curves for apatite ($^{87}Sr/^{86}Sr)_i$ (A) and $\epsilon Nd(t)$ (B), and zircon $\epsilon Hf(t)$ (C) and $\delta^{18}O$ (D) isotopes of the Yulong intrusion. Whole-rock ($^{87}Sr/^{86}Sr)_i$ and $\epsilon Nd(t)$ data from Jiang et al. (2006) and Xu et al. (2016a), and zircon $\epsilon Hf(t)$ data from Jiang et al. (2006), Wang et al. (2011) and Li et al. (2012) are also illustrated in A-C.

relatively high oxygen fugacity during their crystallization. They are characterized by higher SiO_2, MgO, and CaO contents, and lower Al_2O_3, FeO, TiO_2, and NaO_2 contents (Al_2O_3 = 3.47–4.87 wt%; SiO_2 = 49.92–52.05 wt%; Appendix Table A4; Fig. 11A–F), and are mainly classified as tremolite (Fig. 12A; Hawthorne et al., 2012).

Amphibole compositions can be used to estimate oxidation states and water contents of the magma from which the amphibole crystallized, and crystallization temperatures and pressures of the amphibole (e.g., Duan and Jiang, 2017; Leng et al., 2018; Zhu et al., 2018). The estimated magmatic oxidation states, water contents (using the spreadsheet of Ridolfi et al., 2010), crystallization temperatures (using the equation of Ridolfi and Renzulli, 2012) and pressures (using the spreadsheet of Mutch et al., 2016) of the amphibole grains from Yulong are listed in Appendix Table A4 and illustrated Fig. 12B–D. The parental magma to early-stage amphibole grains has crystallization temperatures ranging from 629° to 722 °C (average = 669° ± 22 °C, n = 25), pressures from 1.9 to 3.3 kbars (average = 2.5 ± 0.4 kbars, n = 25), water contents from 3.5 to 4.6 wt% (average = 4.2 ± 0.3 wt%, n = 25), and ΔNNO (where NNO is the Ni-NiO buffer) from 0.6 to 1.5 (average = 1.1 ± 0.2, n = 25). Crystallization depth of early-stage amphibole grains, assuming conditions of lithostatic pressure (ρ_{crust} = 2.7 × 10^3 kg/m^3), are 7.1–12.5 km (average = 9.5 ± 1.4 km, n = 25), which indicate that they may have crystallized in the underlying magma chamber (5–15 km; Cloos, 2001; Richards, 2005; Sillitoe, 2010). By contrast, the parental magma to late-stage amphibole grains has crystallization temperatures from 559° to 617 °C (average = 595° ± 19 °C, n = 8), pressures from 1.0 to 1.5 kbars (average = 1.3 ± 0.2 kbars, n = 8), water contents from 2.8 to 3.5 wt% (average = 3.2 ± 0.2 wt%, n = 8), and ΔNNO from 1.9 to 2.3

(average = 2.1 ± 0.1, n = 8). Crystallization depth of late-stage amphibole grains are 4.0–5.6 km (average = 4.8 ± 0.6 km, n = 8), suggesting that they probably crystallized in the porphyritic stock (2–5 km; Cloos, 2001; Seedorff et al., 2005; Sillitoe, 2010) that roots in the underlying magma chamber.

In this study, the least-altered samples were petrographically examined, and only fresh amphibole grains from the least-altered samples were selected for electron microprobe analysis. We therefore consider that alteration may only have had a minimal effect on the compositions of amphiboles, as well as on the caculated crystallizing physical-chemical conditions such as pressure and magmatic oxygen fugacity.

4.4.2. Plagioclase compositions

Three least-altered plagioclase phenocrysts were analyzed to reveal the variations of chemical compositions from core to rim. The results show that these phenocrysts have complex and repeated zonings in anorthite (An) contents, which are coupled by FeO contents (Appendix Table A5; Fig. 13A–C). One plagioclase crystal from sample ZK1007-454 is characterized by repeated zonings, with An and FeO contents decrease from core to mantle, and then increase but finally decrease in the rim (Fig. 13A). Another plagioclase crystal from sample ZK1007-454 almost shows reverse zoning, with the An and FeO contents finally decrease in the rim (Fig. 13B). The plagioclase crystal from sample ZK1007-660 is characterized by saw-toothed core-to-rim An contents variations (Fig. 13C). Overall, the plagioclase phenocrysts have An contents ranging from 16 to 41 mol% (average = 26 ± 6 mol%, n = 22), and are classified as oligoclase (An$_{10-20}$) to andesine (An$_{40-50}$).

Table 2
Summary of in-situ apatite Sr–Nd isotopic compositions of the Yulong intrusion.

Sample	$^{87}Rb/^{86}Sr$	2σ	$^{87}Sr/^{86}Sr$	2σ	$(^{87}Sr/^{86}Sr)_i$	2σ	$^{147}Sm/^{144}Nd$	2σ	$^{143}Nd/^{144}Nd$	2σ	$\epsilon Nd(t)$
ZK0807-220	0.0010	0.0001	0.7065	0.0001	0.7065	0.0001	0.1065	0.0001	0.51248	0.00005	−2.7
ZK0807-100	0.0024	0.0002	0.7065	0.0002	0.7065	0.0001	0.1273	0.0002	0.51250	0.00004	−2.4
ZK0807-30	0.0017	0.0001	0.7065	0.0001	0.7065	0.0001	0.1329	0.0003	0.51250	0.00004	−2.4
ZK0812-275	0.0010	0.0001	0.7066	0.0001	0.7066	0.0001	0.1060	0.0001	0.51246	0.00005	−3.0
YL1525	0.0023	0.0003	0.7065	0.0003	0.7065	0.0003	0.1192	0.0003	0.51250	0.00005	−2.3
ZK1007-671	0.0010	0.0001	0.7062	0.0001	0.7062	0.0001	0.0799	0.0001	0.51249	0.00004	−2.2
ZK1007-771	0.0021	0.0003	0.7063	0.0003	0.7063	0.0002	0.0774	0.0001	0.51252	0.00005	−1.7

Note: The following values are used to calculate the initial Sr ($(^{87}Sr/^{86}Sr)_i$) and Nd ($\epsilon Nd(t)$) isotopic compositions: age = 41 Ma (Liang et al., 2006; Li et al., 2012); $\lambda_{Rb} = 1.42 \times 10^{-11}$ year^{-1} (Steiger and Jager, 1977); $\lambda_{Sm} = 6.54 \times 10^{-12}$ year^{-1} (Lugmair and Marti, 1978); $(^{143}Nd/^{144}Nd)_{CHUR} = 0.512638$ (Goldstein et al., 1984); $(^{147}Sm/^{144}Nd)_{CHUR} = 0.1967$ (Jacobsen and Wasserburg, 1980). Two-stage Nd model age (T_{DM2}) is calculated using the same formulation as Keto and Jacobsen (1987).

5. Discussion

5.1. Origin of the Yulong intrusion

The Yulong intrusion has mainly positive zircon $\epsilon Hf(t)$ values (0.5−8) and young Hf mantle model ages (Figs. 8C and 9A; Table 3), suggesting its origin from a depleted or juvenile source. It has been suggested that the Yulong intrusion originated directly from low-degree partial melting of a metasomatized lithospheric mantle (Jiang et al., 2006), or formed by assimilation-fractional crystallization (AFC) of metasomatized mantle-derived melts (Hou et al., 2003; Xu et al., 2016a). However, the high whole-rock SiO_2 (66.3−69.5 wt%) and low MgO (<1.24%) contents and Mg# values (<46) argue against its origin by direct partial melting of the lithosphere mantle (Baker et al., 1995; Martin et al., 2005). Felsic magmas could be generated via assimilation-fractional crystallization (AFC) and/or fractional crystallization (FC) processes of mafic magmas (Miller et al., 1999). Although a few inherited zircons have been found in the Yulong intrusion (Li et al., 2012), the relatively uniform zircon Hf−O and apatite Sr−Nd isotopes (Figs. 8 and 9) probably indicate that crustal contamination is insignificant during emplacement of Yulong. An alternative explanation for origin of the Yulong intrusion is the fractional crystallization of a mantle-derived mafic magma. Lithospheric mantle-derived mafic lavas coeval with the Yulong intrusion are widely developed in the Nangqian Basin (Deng et al., 2001; Spurlin et al., 2005), which is about 100 km NW of Yulong (Fig. 1B). They have less evolved Sr−Nd isotopes (Fig. 9B), but remarkably higher REE and LILEs contents than the Yulong intrusion (Fig. 7A−B). This suggests that these mafic lavas are unlikely to have been the parental magma of the Yulong intrusion, because fractional crystallization of a mafic magma generally produce felsic magmas with higher REE and LILEs contents (e.g., Rollison, 1993).

The depleted source of the Yulong intrusion is probably a juvenile mafic lower arc crust, as suggested by the arc-like trace element patterns (Fig. 7A−B) and positive zircon Hf isotopes and young Hf mantle model ages (Figs. 8C, and 10). These Hf isotopes and model ages overlap those of Paleo-Tethys subduction-related arc magmas in the north Qiangtang terrane (Fig. 10; Zi et al., 2012b). In addition, the relatively low contents of highly compatible elements (e.g., Cr) and low Mg# values at Yulong are comparable to those of thick lower-crust derived adakite-like rocks (Fig. 6B−D), which also indicates its origin from partial melting of the thickened lower crust (Wang et al., 2006). Furthermore, the Yulong intrusion has mainly elevated zircon $\delta^{18}O$ values of 6.4 to 7.6‰ (Figs. 8D and 9A; average = 7.0 ± 0.5‰, 2σ, $n = 79$). These values are similar to average value of the global lower crust ($\delta^{18}O = 7.0$‰; Kempton and Harmon, 1992), but significantly higher than the values of mantle (5.3 ± 0.6‰, 2σ, Valley et al., 1998, 2005), and higher than the magmas that predominately derived from fractional crystallization of mantle-derived parental melts (<6.5‰; Valley et al., 2005). This indicates that the Yulong intrusion should not have originated from the lithospheric mantle, but most likely from the juvenile mafic lower crust.

It is also noteworthy that a few magmatic zircons at Yulong have negative zircon $\epsilon Hf(t)$ and high $\delta^{18}O$ values (Figs. 8C−D, 9A, and 10; Jiang et al., 2006; Li et al., 2012). This probably indicates a heterogeneous source of the Yulong intrusion, consisting mainly of a juvenile mafic lower crust with positive $\epsilon Hf(t)$ values and an ancient crustal component with negative $\epsilon Hf(t)$ values and high $\delta^{18}O$ values. The ancient crustal component is probably metasedimentary rocks, as suggested by the elevated zircon $\delta^{18}O$ (>7.8‰) values (Figs. 8D and 9A). These high $\delta^{18}O$ values are typical of supracrustal input (Cavosie et al., 2005; Hawkesworth and Kemp, 2006; Kemp et al., 2006). The Sr−Nd isotopes of the Yulong intrusion plot between juvenile lower arc crust (as isotopically approximated by Paleo-Tethys subduction-related tonalite from Zi et al., 2012b) and the ancient lower crust (as approximated by ancient sedimentary rocks-derived S-type granites from Wu et al.,
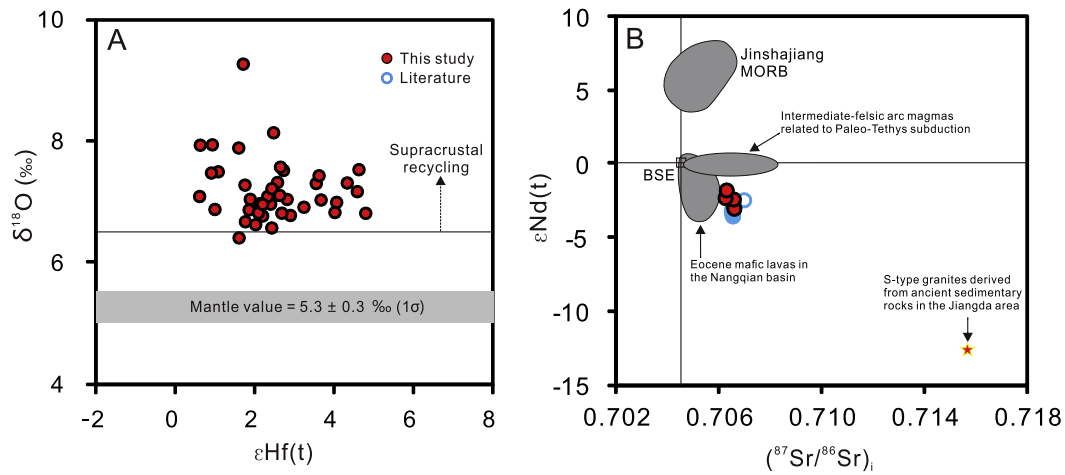
Fig. 9. Histograms of zircon δ¹⁸O vs. εHf(t) (A) and apatite (⁸⁷Sr/⁸⁶Sr)ᵢ vs. εNd(t) (B) for the Yulong intrusion. The δ¹⁸O values for mantle zircons are from Valley et al. (1998, 2005), whereas the δ¹⁸O values indicating supracrustal recycling are from Cavosie et al. (2005) and Hawkesworth and Kemp (2006). Data for intermediate-felsic arc magmas related to Paleo-Tethys Ocean subduction are from Zi et al. (2012b) and Wu et al. (2013). Data for S-type granites derived from ancient sedimentary rocks are from Wu et al. (2013). Data for Eocene mafic lavas in the Nangqian basin are from Deng et al. (2001) and Spurlin et al. (2005). Data sources of Yulong are the same as those in Fig. 8. BSE = Bulk silicate earth.

Table 3
Zircon Hf and O isotopic compositions of the Yulong intrusion.

Analyses	$^{176}Lu/^{177}Hf$	2σ	$^{176}Hf/^{177}Hf$	2σ	$^{176}Yb/^{177}Hf$	2σ	εHf(t)	ƒ(Lu/Hf)	$T_{DM,2}$(Ma)	δ¹⁸O	2σ
YL912@1	0.0012	0.0000	0.282818	0.000019	0.03	0.00	2.5	−0.96	955.7	7.3	0.3
YL912@2	0.0010	0.0000	0.282814	0.000015	0.02	0.00	2.4	−0.97	964.9	6.6	0.3
YL912@3	0.0008	0.0000	0.282795	0.000014	0.02	0.00	1.7	−0.98	1007.4	6.7	0.3
YL912@4	0.0010	0.0000	0.282798	0.000014	0.02	0.00	1.8	−0.97	1001.4	6.9	0.2
YL912@5	0.0010	0.0000	0.282868	0.000016	0.02	0.00	4.3	−0.97	843.4	7.3	0.3
YL912@6	0.0008	0.0000	0.282793	0.000027	0.02	0.00	1.6	−0.98	1010.9	9.3	0.3
YL912@7	0.0011	0.0000	0.282776	0.000017	0.03	0.00	1.0	−0.97	1051.0	7.5	0.3
YL912@8	0.0013	0.0000	0.282813	0.000015	0.03	0.00	2.3	−0.96	966.6	7.0	0.3
YL912@9	0.0010	0.0000	0.282763	0.000017	0.03	0.00	0.6	−0.97	1079.8	8.0	0.4
YL912@10	0.0009	0.0000	0.282811	0.000015	0.02	0.00	2.3	−0.97	971.5	7.1	0.2
YL912@11	0.0009	0.0000	0.282815	0.000016	0.02	0.00	2.4	−0.97	962.0	8.2	0.2
YL912@12	0.0010	0.0000	0.282849	0.000016	0.02	0.00	3.6	−0.97	885.7	7.1	0.3
YL912@13	0.0009	0.0000	0.282822	0.000019	0.02	0.00	2.6	−0.97	946.1	7.5	0.2
YL912@14	0.0012	0.0000	0.282790	0.000016	0.03	0.00	1.5	−0.97	1018.1	7.9	0.2
YL912@15	0.0008	0.0000	0.282814	0.000015	0.02	0.00	2.4	−0.98	964.8	7.2	0.2
YL912@16	0.0011	0.0000	0.282825	0.000017	0.03	0.00	2.7	−0.97	940.3	7.1	0.3
YL912@17	0.0011	0.0000	0.282846	0.000017	0.03	0.00	3.5	−0.97	893.5	7.3	0.3
YL912@18	0.0009	0.0000	0.282805	0.000016	0.02	0.00	2.0	−0.97	985.6	7.0	0.3
YL912@19	0.0012	0.0000	0.282771	0.000016	0.03	0.00	0.8	−0.96	1061.9	7.5	0.4
YL912@20	0.0012	0.0000	0.282772	0.000017	0.03	0.00	0.9	−0.96	1060.3	8.0	0.4
YL912@21	0.0012	0.0000	0.282876	0.000016	0.03	0.00	4.6	−0.96	824.6	7.6	0.2
YL912@22	0.0012	0.0000	0.282820	0.000018	0.03	0.00	2.6	−0.96	951.9	7.1	0.3
YL912@23	0.0011	0.0000	0.282875	0.000019	0.03	0.00	4.5	−0.97	827.3	7.2	0.2
YL912@24	0.0009	0.0000	0.282799	0.000015	0.02	0.00	1.8	−0.97	999.5	7.1	0.4
YL906@1	0.0009	0.0000	0.282829	0.000014	0.02	0.00	2.9	−0.97	931.9	6.8	0.3
YL906@2	0.0008	0.0000	0.282807	0.000018	0.02	0.00	2.1	−0.98	980.4	7.0	0.3
YL906@3	0.0011	0.0000	0.282862	0.000026	0.03	0.00	4.0	−0.97	857.6	7.0	0.2
YL906@4	0.0010	0.0000	0.282849	0.000018	0.03	0.00	3.6	−0.97	885.8	7.5	0.3
YL906@5	0.0011	0.0000	0.282809	0.000016	0.03	0.00	2.2	−0.97	976.6	6.8	0.4
YL906@6	0.0008	0.0000	0.282775	0.000023	0.02	0.00	1.0	−0.98	1053.3	6.9	0.3
YL906@7	0.0012	0.0000	0.282764	0.000017	0.03	0.00	0.6	−0.96	1077.9	7.1	0.2
YL906@8	0.0010	0.0000	0.282882	0.000018	0.03	0.00	4.8	−0.97	810.7	6.8	0.3
YL906@9	0.0010	0.0000	0.282821	0.000019	0.03	0.00	2.6	−0.97	947.9	7.6	0.4
YL906@10	0.0009	0.0000	0.282804	0.000016	0.02	0.00	2.0	−0.97	987.8	6.6	0.4
YL906@11	0.0012	0.0000	0.282806	0.000017	0.03	0.00	2.1	−0.96	983.5	6.8	0.4
YL906@12	0.0010	0.0000	0.282792	0.000018	0.02	0.00	1.6	−0.97	1014.5	6.4	0.2
YL906@13	0.0007	0.0000	0.282809	0.000018	0.02	0.00	2.2	−0.98	976.5	7.0	0.3
YL906@14	0.0011	0.0000	0.282796	0.000017	0.03	0.00	1.7	−0.97	1005.0	7.3	0.4
YL906@15	0.0011	0.0000	0.282823	0.000014	0.03	0.00	2.7	−0.97	945.7	6.8	0.3
YL906@16	0.0011	0.0000	0.282838	0.000017	0.03	0.00	3.2	−0.97	910.1	6.9	0.4
YL906@17	0.0010	0.0000	0.282860	0.000016	0.03	0.00	4.0	−0.97	860.3	6.8	0.2

Note: The εHf(t) values are calculated using present-day $(^{176}Lu/^{177}Hf)_{CHUR} = 0.0332$ and $(^{176}Hf/^{177}Hf)_{CHUR} = 0.282772$ (Blichert-Toft and Albarède, 1997). T_{DM2} values are calculated using present-day $(^{176}Lu/^{177}Hf)_{DM} = 0.0384$ and $(^{176}Hf/^{177}Hf)_{DM} = 0.28325$ (Griffin et al., 2000). Decay constant of ^{176}Lu is 1.865×10^{-11} yr^{-1} (Scherer et al., 2001). $^{176}Hf/^{177}Hf$ value for the average continental crust is 0.015 (Griffin et al., 2002).
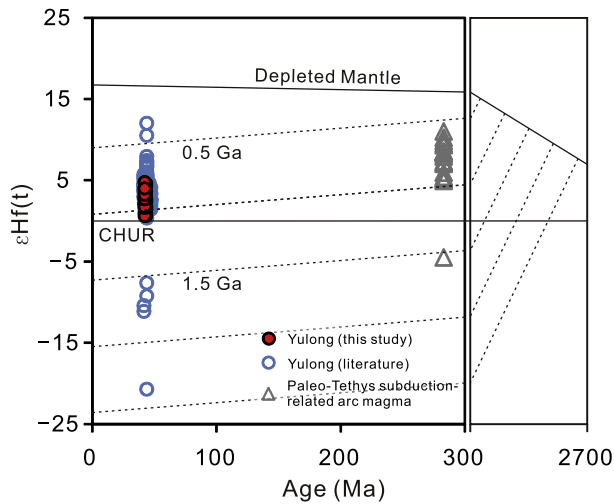
Fig. 10. Plots of zircon ages vs. zircon εHf(t) values of the Yulong intrusion and the Paleo-Tethys Ocean subduction-related magmas in the north Qiangtang terrane. Data for the Yulong intrusion are from Jiang et al. (2006), Wang et al. (2011), Li et al. (2012), and this study. Data for the Paleo-Tethys Ocean subduction-related magmas in north Qiangtang terrane are from Zi et al. (2012b).

2013) in the north Qiangtang terrane (Fig. 9B), which further suggests its origin by mixing between the juvenile and old crust. Mixing of ancient- and juvenile crustal components could have happened in the source, or by magma mixing during emplacement. It has been suggested that efficient hybridization between mafic and felsic magmas could only happen under the conditions of high temperature and intense magma convection in depth (Chen et al., 2009). This, together with the deficiency of covariant between zircon εHf(t) and $\delta^{18}O$ values (Fig. 7A) and homogeneous Sr–Nd isotopes (Fig. 7B), indicates that the mixing of ancient- and juvenile crustal components was most likely to have happened in the deep crust by concurrent partial melting.

The Yulong intrusion has broadly similar zircon U–Pb ages (~41.0 Ma; Liang et al., 2006; Li et al., 2012; Huang et al., 2019b) and geochemical features with the alkaline felsic magmatic rocks along the strike-slip faults in eastern Tibet and western Yunnan (i.e. the Jinshajiang-Ailaoshan belt; 43.8–34.6 Ma; e.g., Zhang and Xie, 1997; Wang et al., 2001; Bi et al., 2004, 2005; Hu et al., 2004; Hou et al., 2006; Liang et al., 2006, 2007; Xu et al., 2012, 2016a; Lu et al., 2013; Yang et al., 2014a, 2014b; Campbell et al., 2014; He et al., 2016). This indicates that they may have formed in similar geodynamic setting. Although partial melting of sources of these alkalic-rich igneous rocks has been attributed to asthenospheric
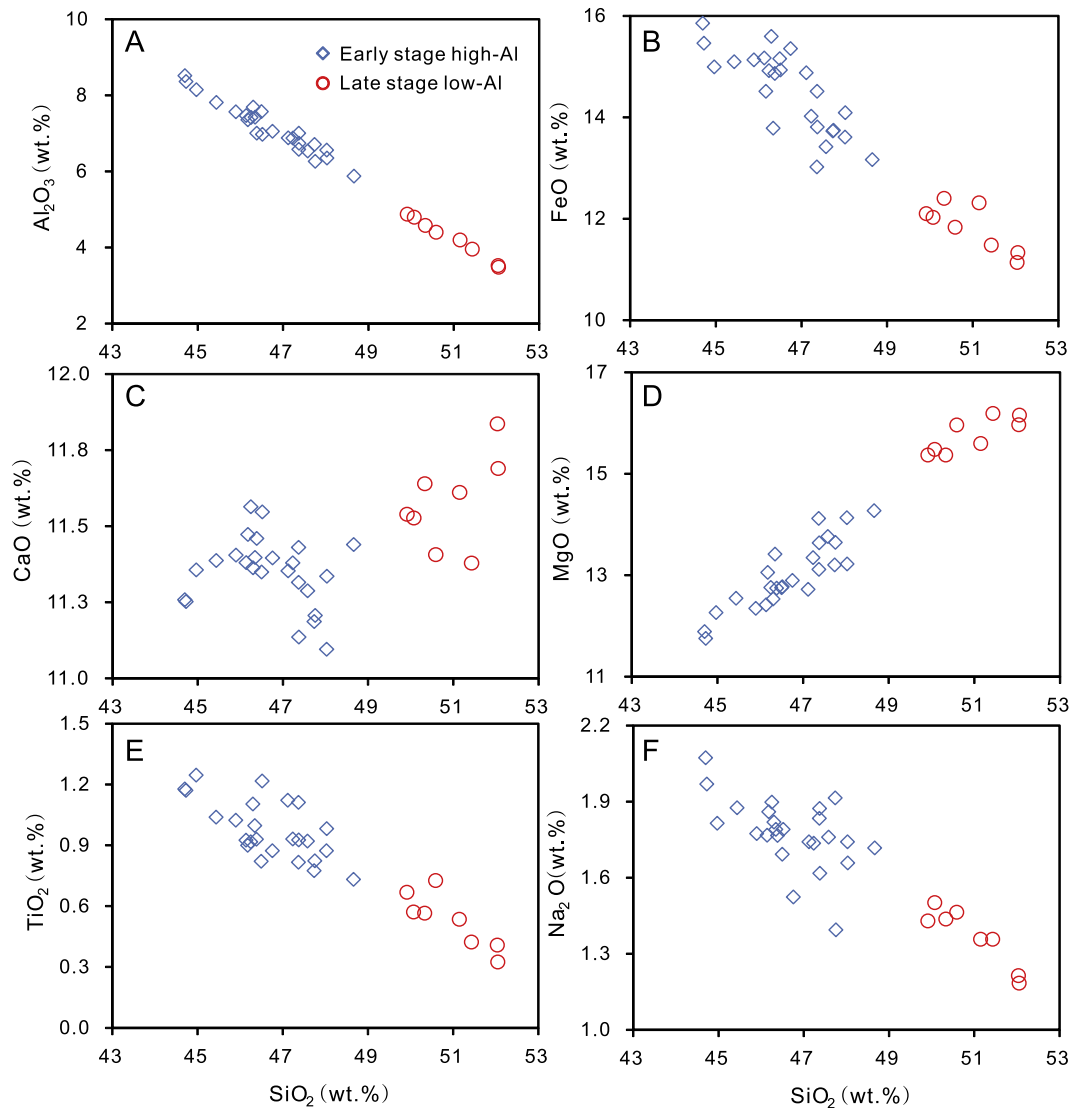

Fig. 11. Plots of major element compositions of amphibole from the Yulong intrusion. A. Al_2O_3 vs. SiO_2. B. FeO vs. SiO_2. C. CaO vs. SiO_2. D. MgO vs. SiO_2. E. TiO_2 vs. SiO_2. F. Na_2O vs. SiO_2.
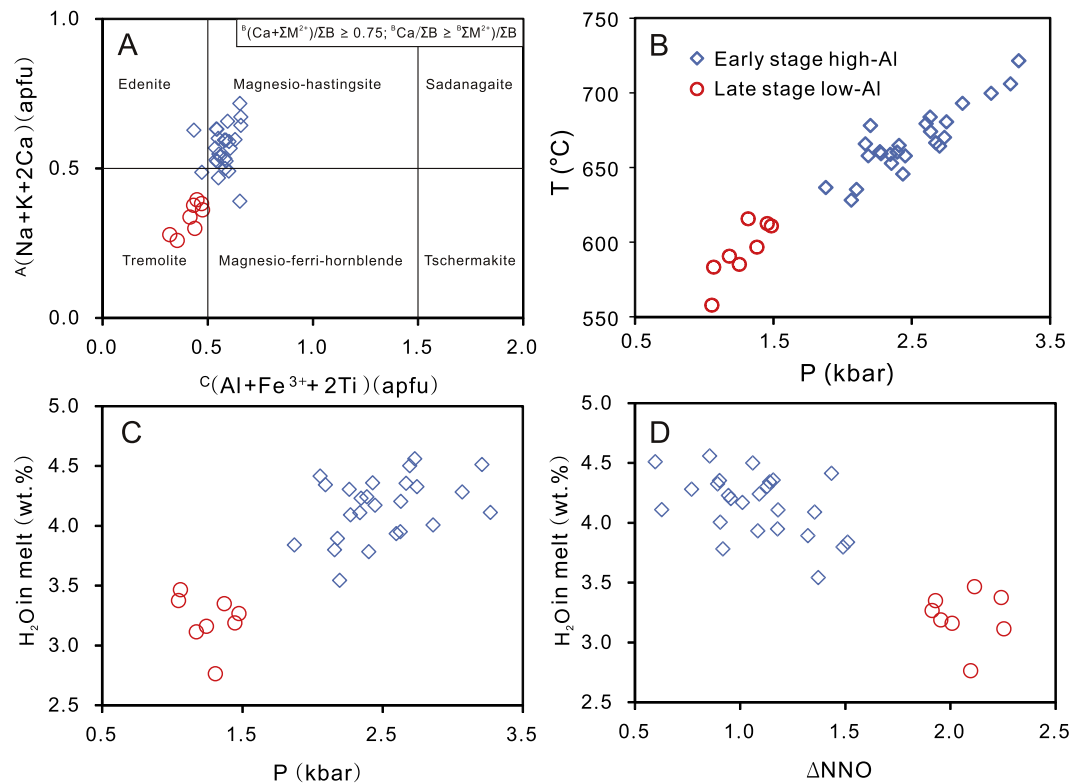
Fig. 12. Discrimination diagram and plots of crystallization pressure, temperature, oxidation state (ΔNNO), and magmatic water content estimated from amphibole compositions from the Yulong deposit. A. ^{A}(Na + K +2Ca)(apfu) vs. ^{C}(Al + Fe^{3+} +2Ti)(apfu) (Hawthorne et al., 2012). B. Temperature (°C) vs. pressure (kbar). C. Magmatic water contents (wt%) vs. pressure (kbar). D. Magmatic water contents (wt%) vs. ΔNNO. The atomic proportions of amphibole were caculated by using the spreadsheet given by Locock (2014). The magmatic oxidation states (ΔNNO) and magmatic water content were caculated by using the spread sheet of Ridolfi et al. (2010). The crystallization temperature were caculated using the equation of Ridolfi and Renzulli (2012). The crystallization pressure was caculated by using the equation of Mutch et al. (2016). Abbreviation: apfu = atoms per formula unit.

upwelling (e.g., Zhang and Xie, 1997), the cause of asthenospheric upwelling remains controversial. Several models have been proposed for these disputes, including delamination of the lithospheric mantle (e.g., Lu et al., 2013; He et al., 2016), and the regional decompression caused by strike-slip fault systems (Hou et al., 2003; Xu et al., 2016a). Considering the fact that the Cenozoic alkaline magmatic rocks (including the Yulong intrusion) are distributed strictly along the NW-SE strike-slip faults, we prefer the later model that asthenospheric upwelling was induced by regional decompression caused by strike-slip faults. Therefore, the partial melting of ancient- and juvenile crustal components at Yulong was probably triggered by crustal scale extension and upwelling of the asthenosphere along the strike-slip faults in eastern Tibet (Zhang and Xie, 1997; Wang et al., 2001; Hou et al., 2003), caused by India-Asia collision at about 65–55 Ma (Fig. 14A–B; Chung et al., 1997; Leech et al., 2005; Mo et al., 2007; Hu et al., 2015b).

5.2. Replenishment in the magma chamber

Plagioclase phenocrysts from Yulong show large variation of An contents of up to 25 mol% (Fig. 13A–C; Appendix Table A5). The An contents vary periodically or conversely from plagioclase cores to rims, and are coupled by FeO contents (Fig. 13A–C). These large-scale (100 μm~) An and FeO variations are unlikely to have been caused by simple changes in magma pressure/temperatures or by chemical diffusion (Singer et al., 1995; Ustunisik et al., 2014; Waters and Lange, 2015), but probably reflect periodic changes in magma compositions (Singer et al., 1995; Andrews et al., 2008; Cao et al., 2014; Zhu et al., 2018). The periodic changes in magma compositions are most possibly resulted from pulsed recharge of the magma chamber by a less evolved magma (Singer et al., 1995; Rohalach and Loucks, 2005; Andrews et al., 2008; Cao et al., 2014,

2018). This interpretation is consistent with the conclusion based on periodic sulfur zonation in apatite crystals at Yulong (Huang et al., 2019b), and is also in agreement with the repeated exsolution of compositionally similar ore-forming fluids (Chang et al., 2018).

5.3. Fluid exsolution in the magma chamber

The early-stage amphibole phenocrysts from Yulong have higher crystallization pressures and temperatures than the late-stage amphibole grains, suggesting that they crystalized at deeper depth before the crystallization of low-Al amphiboles (Fig. 12B). Caculated crystallization depths indicate that the early-stage amphibole may have crystallized in the underlying magma chamber (7.1–12.5 km), whereas the low-Al amphibole has crystallized in the porphyry stock (4.0–5.6 km). Caculated water contents of the magma parental to the late-stage amphibole are lower than those of the early-stage amphibole, which may suggest fluid exsolution from the underlying magma chamber at the time of emplacement of the Yulong stock (Fig. 12C; Leng et al., 2018; Zhu et al., 2018). Furthermore, the late-stage amphiboles have higher magmatic oxygen fugacities (e.g., ΔNNO values) than the early-stage amphiboles (Fig. 12D). This is possibly caused by late-stage fractionation or fluid exsolution process, as the caculated fO2 values are negatively correlated with water contents (Fig. 12D). Nonetheless, it should be noted that the magmatic oxidation states are high throughout the magmatic evolution (ΔNNO > 0.5), which is consistent with the conclusion based on zircon trace element compositions (Liang et al., 2006; Xu et al., 2016a). The elevated oxygen fugacity will suppress early formation of Cu-rich sulfides, and thus will be favorable for metal transportation and enrichment during magma evolution and emplacement (Mungall, 2002; Jugo et al., 2005; Richards, 2015).
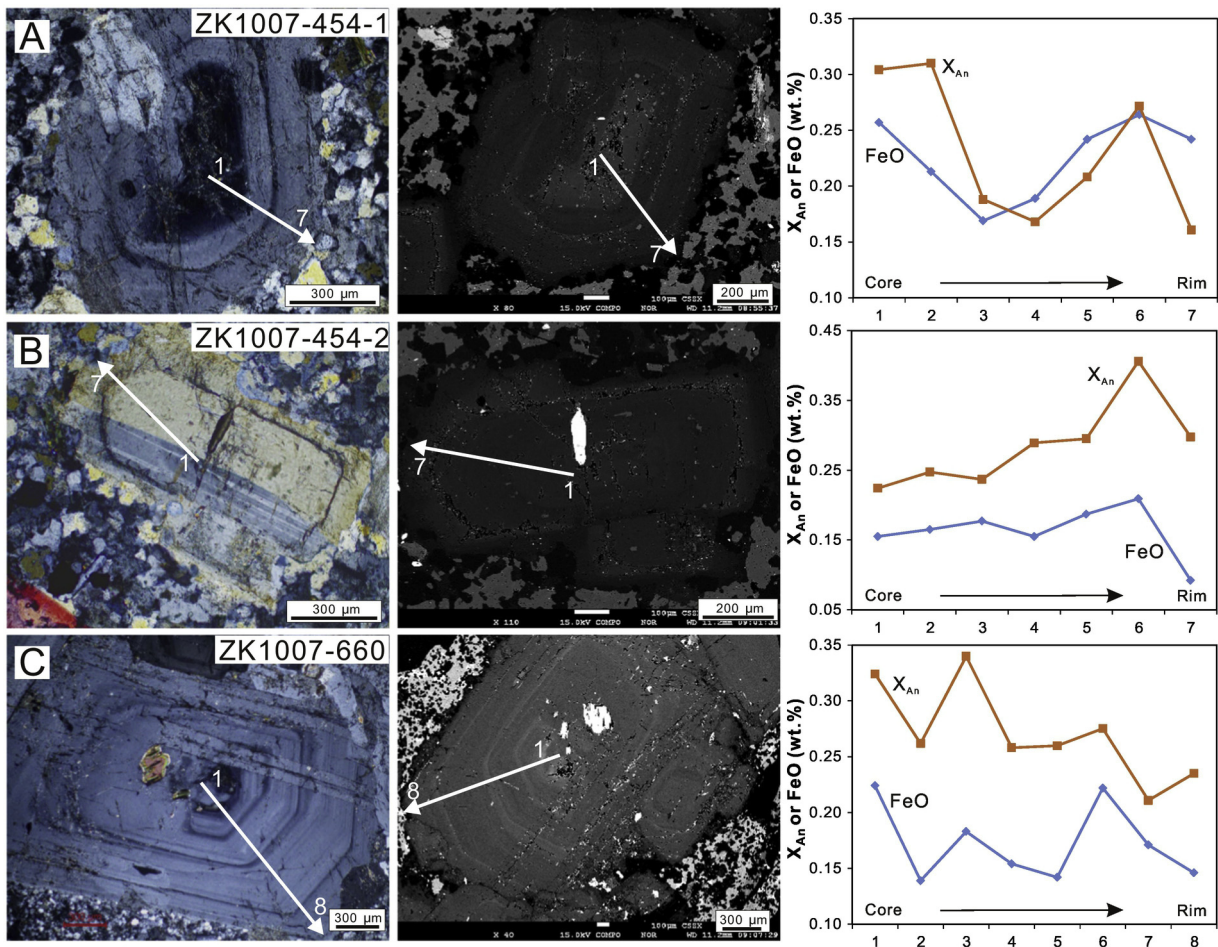
Fig. 13. Cross-polarized transmitted light microphotographs, backscattered electron (BSE) images, and core-to-rim transects showing variations of anorthite proportion (X_{An}) and FeO contents of representative plagioclase phenocrysts from the Yulong intrusion.

In summary, the magma chamber beneath Yulong might have been recharged by a compositionally less evolved magma, and was saturated in magmatic fluid before or coeval with the emplacement of the Yulong stock in the magma chamber. The magmatic oxidation states are high, and increase during magma evolution, which may have been essential to the enrichment of metals in the evolving magma.

6. Conclusions

The Yulong intrusion has homogenous apatite Sr–Nd isotopes ((^{87}Sr/^{86}Sr)$_i$ = 0.7060–0.7068; ϵNd(t) = −4.8−0.2) that plot between juvenile and ancient crust in eastern Tibet. Zircon grains from this study and published studies have mainly positive yet
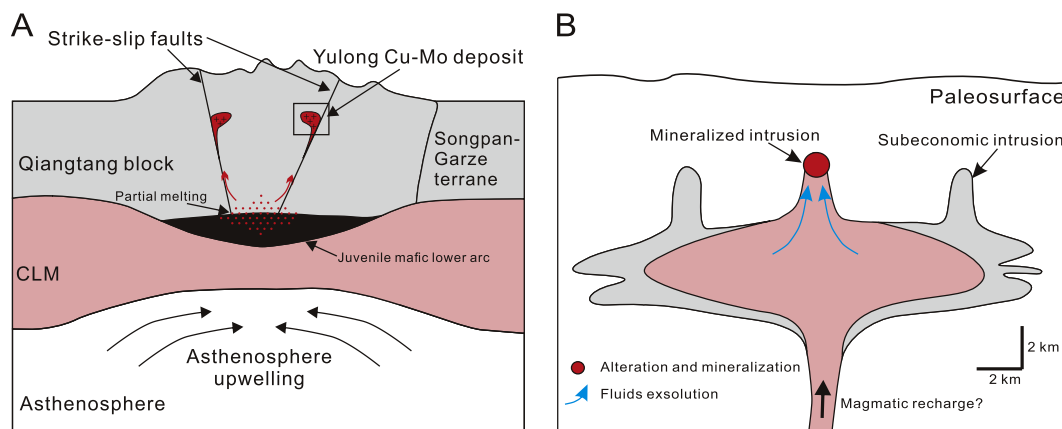

Fig. 14. Origin and ore-forming process of the postsubduction Yulong porphyry Cu–Mo deposit. A. The India-Asia collision-related strike-slip faults caused upwelling of the asthenosphere, which provided heat for remelting of the sulfide-bearing residues of former arc magmas and ancient crustal materials. The resultant magmas migrated to middle-upper crustal levels along the crustal-scale strike-slip faults to form the underlying magma chamber. B. The magma chamber beneath Yulong might have been recharged by a mafic magma, and was saturated in magmatic fluids to produce intensive hydrothermal alteration and mineralization.

variable ϵHf(t) values (−20.6 to +12.2) and elevated $\delta^{18}O$ values (6.4 to 9.3‰). These Sr-Nd-Hf-O isotopes, in combined with the high whole-rock SiO_2 (66.3–69.5 wt%) contents and La/Yb ratios (36.4–68.0), low MgO (0.63–1.24%) and Cr (<30 ppm) contents, and the arc-like trace element patterns, suggest that the Yulong intrusion may have originated from concurrent partial melting of Paleo-Tethys subduction-related juvenile lower arc crust and a small amount of ancient crustal materials.

Textural and compositional variations of silicate mineral phenocrysts (amphibole, plagioclase) suggest that the magma chamber beneath Yulong (7.1–12.5 km in depth) might have been recharged by a mafic magma, and was saturated in magmatic fluids at the time of emplacement of the Yulong intrusion (4.0–5.6 km in depth). The oxidation states are relatively high (ΔNNO >0.6), and increase through magma evolution. This temporal variation of oxidation states allows the metals to be enriched in the magma during magma evolution, and to be deposited in the hydrothermal alteration stage.

Appendix A. Supplementary data

Supplementary data to this article can be found online at https://doi.org/10.1016/j.gr.2019.05.012.

References

Andrews, B.J., Gardner, J.E., Housh, T.B., 2008. Repeated recharge, assimilation, and hybridization in magmas erupted from El Chichón as recorded by plagioclase and amphibole phenocrysts. J. Volcanol. Geotherm. Res. 175, 415–426.

Baker, M., Hirschmann, M., Ghiorso, M., Stolper, E., 1995. Compositions of near-solidus peridotite melts from experiments and thermodynamic calculations. Nature 375, 308–311.

Ballard, J.R., Palin, M.J., Campbell, I.H., 2002. Relative oxidation states of magmas inferred from Ce(IV)/Ce(III) in zircon: application to porphyry copper deposits of northern Chile. Contrib. Mineral. Petrol. 144, 347–364.

Bi, X.W., Hu, R.Z., Cornell, D.H., 2004. The alkaline porphyry associated Yaotsm gold deposit, Yunnan, China: rare earth element and stable isotope evidence for magmatichydrothermal ore formation. Miner. Deposita 39, 21–30.

Bi, X.W., Hu, R.Z., Peng, J.T., Wu, K.X., Su, W.C., Zhan, X.Z., 2005. Geochemical characteristics of the Yao'an and Machangqing alkaline-rich intrusions. Acta Petrol. Sin. 21, 113–124 (in Chinese with English abstract).

Burnham, C.W., 1979. Magmas and hydrothermal fluids. In: Barnes, H.L. (Ed.), Geochemistry of Hydrothermal Ore Deposits, 2nd edition. John Wiley and Sons, New York, pp. 71–136.

Campbell, Ian H., Stepanov, A.S., Liang, H.Y., Allen, C.M., Norman, M.D., Zhang, Y.Q., Xie, Y.W., 2014. The origin of shoshonites: new insights from the Tertiary high-potassium intrusions of eastern Tibet. Contrib. Mineral. Petrol. 167, 1–22.

Candela, P.A., 1992. Controls on ore metal ratios in granite-related ore systems: an experimental and computational approach. Transactions of the Royal Society of Edinburgh Earth Sciences 83, 317–326.

Cao, M.J., Qin, K.Z., Li, G.M., Yang, Y.H., Evans, N.J., Zhang, R., Jin, L.Y., 2014. Magmatic process recorded in plagioclase at the Baogutu reduced porphyry Cu deposit, western Junggar, NW-China. J. Asian Earth Sci. 82, 136–150.

Cao, M.J., Hollings, P., Cooke, D.R., Evans, N.J., McInnes, B.I.A., Qin, K.Z., Li, G.M., Sweet, G., Baker, M., 2018. Physicochemical processes in the magma chamber under the Black Mountain porphyry Cu-Au deposit, Philippines: insights from mineral chemistry and implications for mineralization. Econ. Geol. 113 (1), 63–82.

Castillo, P.R., Janney, P.E., Solidum, R.U., 1999. Petrology and geochemistry of Camiguin Island, southern Philippines: Insights to the source of adakites and

other lavas in a complex arc setting. Contrib. Mineral. Petrol. 134, 33–51.

Cavosie, A.J., Valley, J.W., Wilde, S.A., E., I.M.F., 2005. Magmatic $\delta^{18}O$ in 4400–3900 Ma detrital zircons: a record of the alteration and recycling of crust in the Early Archean. Earth Planet. Sci. Lett. 235 (3), 663–681.

Chang, J., Li, J.W., Selby, D., Liu, J.C., Deng, X.D., 2017. Geological and chronological constraints on the long-lived Eocene Yulong porphyry Cu-Mo deposit, eastern Tibet, China: implications for lifespan of magmatic-hydrothermal processes forming giant and supergiant porphyry Cu deposits. Econ. Geol. 112 (7), 1719–1746.

Chang, J., Li, J.W., Audétat, A., 2018. Formation and evolution of multistage magmatic-hydrothermal fluids at the Yulong porphyry Cu-Mo deposit, eastern Tibet: Insights from LA-ICP-MS analysis of fluid inclusions. Geochim. Cosmochim. Acta 232, 181–205.

Chelle-Michou, C., Chiaradia, M., 2017. Amphibole and apatite insights into the evolution and mass balance of Cl and S in magmas associated with porphyry copper deposits. Contributions to Mineralogy and Petrology 172, 105.

Chen, B., He, J.B., Ma, X.H., 2009. Petrogenesis of mafic enclaves from the north Taihang Yanshanian intermediate to felsic plutons: evidence from petrological, geochemical, and zircon Hf-O isotopic data. Science in China 52 (9), 1331–1344.

Chung, S.L., Lee, T.Y., Lo, C.H., Wang, P.L., Chen, C., Yem, N.T., Hoa, T.T., Wu, G.Y., 1997. Intraplate extension prior to continental extrusion along the Ailao Shan Red River shear zone. Geology 25, 311–314.

Chung, S.L., Liu, D.Y., Ji, J.Q., Chu, M.F., Lee, H.Y., Wen, D.J., Lo, C.H., Lee, T.Y., Qian, Q., Zhang, Q., 2003. Adakites from continental collision zones: melting of thickened lower crust beneath southern Tibet. Geology 31, 1021–1024.

Cloos, M., 2001. Bubbling magma chambers, cupolas, and porphyry copper deposits. Int. Geol. Rev. 43, 285–311.

Cooke, D.R., Hollings, P., Walshe, J.L., 2005. Giant porphyry deposits: characteristics, distribution, and tectonic controls. Econ. Geol. 100, 801–818.

Deng, W., Sun, H., Zhang, Y., 2001. Petrogenesis of Cenozoic potassic volcanic rocks in Nangqen Basin. Chinese Journal Geology 36, 304–318 (in Chinese with English abstract).

Deng, J., Wang, Q.F., Li, G.J., Li, Chusi, Wang, C.M., 2014. Tethys tectonic evolution and its bearing on the distribution of important mineral deposits in the Sanjiang region, SW China. Gondwana Res. 26, 419–437.

Deng, J., Wang, Q.F., Li, G.J., 2017. Tectonic evolution, superimposed orogeny, and composite metallogenic system in China. Gondwana Res. 50, 216–266.

Duan, D.F., Jiang, S.Y., 2017. In situ major and trace element analysis of amphiboles in quartz monzodiorite porphyry from the Tonglvshan Cu–Fe (Au) deposit, Hubei Province, China: insights into magma evolution and related mineralization. Contrib. Mineral. Petrol. 172 (5), 36.

Gao, Y.F., Hou, Z.Q., Kamber, B.S., Wei, R.H., Meng, X.J., Zhao, R.S., 2007. Adakite-like porphyries from the southern Tibetan continental collision zones: evidence for slab melt metasomatism. Contrib. Mineral. Petrol. 153, 105–120.

Gao, Y.F., Yang, Z.S., Santosh, M., Hou, Z.Q., Wei, R.H., Tian, S.H., 2010. Adakitic rocks from slab melt-modified mantle sources in the continental collision zone of southern Tibet. Lithos 119, 651–663.

Goldstein, S.L., O'Nions, R.K., Hamilton, P.J., 1984. A Sm-Nd isotopic study of atmospheric dusts and particulates from major river systems. Earth and Planetary Science Letters 70, 221–236.

Griffin, W.L., Pearson, N.J., Belousova, E., Jackson, S.E., van Achterbergh, E., O'Reilly, S.Y., Shee, S.R., 2000. The Hf isotope composition of cratonic mantle: LAM-MC-ICPMS analysis of zirconmegacrysts in kimberlites. Geochim. Cosmochim. Acta 64, 133–147.

Griffin, W.L., Wang, X., Jackson, S.E., Pearson, N.J., O'Reilly, S.Y., Xu, X.S., Zhou, X.M, 2002. Zircon chemistry and magmamixing, SE China: in-situ analysis of Hf isotopes, Tonglu and Pingtan igneous complexes. Lithos 61, 237–269.

Guo, L.G., Liu, Y.P., Xu, W., Zhang, X.C., Qin, K.Z., Li, T.S., Shi, Y.R., 2006. Constraints to the mineralization age of the Yulong porphyry copper deposit from SHRIMP U-Pb zircon data in Tibet. Acta Petrol. Sin. 22, 1009–1016 (in Chinese with English abstract).

Hawkesworth, C.J., Kemp, A.I.S., 2006. Using hafnium and oxygen isotopes in zircons to unravel the record of crustal evolution. Chem. Geol. 226 (3–4), 144–162.

Hawkesworth, C., Gallagher, K., Hergt, J., McDermott, F., 1993. Mantle and slab contributions in arc magmas. Annual Review of Earth and Planetary Sciences 21, 175–204.

Hawthorne, F.C., Oberti, R., Harlow, G.E., Maresch, W.V., Martin, R.F., Schumacher, J.C., Welch, M.D., 2012. IMA report: Nomenclature of the amphibole supergroup. Am. Mineral. 97, 2031–2048.

He, W.Y., Mo, X.X., Yang, L.Q., Xing, Y.L., Dong, G.C., Yang, Z., Gao, X., Bao, X.S., 2016. Origin of the Eocene porphyries and mafic microgranular enclaves from the Beiya porphyry Au polymetallic deposit, western Yunnan, China: implicationsfor magma mixing/mingling and mineralization. Gondwana Res. 40, 230–248.

He, W.Y., Yang, L.Q., Lu, Y.J., Jeon, H., Xie, S.X., Gao, X., 2018. Zircon U–Pb dating, geochemistry and Sr–Nd–Hf–O isotopes for the Baimaxueshan granodiorites and mafic microgranulars enclaves in the Sanjiang Orogen: evidence for westward subduction of Paleo-Tethys. Gondwana Res. 62, 112–126.

Hou, Z.Q., Zhang, H.R., 2015. Geodynamics and metallogeny of the eastern Tethyan metallogenic domain. Ore Geol. Rev. 70, 346–384.

Hou, Z.Q., Ma, H., Zaw, K., Zhang, Y.Q., Wang, M.J., Wang, Z., Pan, G.T., Tang, R.L., 2003. The Himalayan Yulong porphyry copper belt: product of large-scale strike-slip faulting in eastern Tibet. Econ. Geol. 98 (1), 125–145.

Hou, Z.Q., Gao, Y.F., Qu, X.M., Rui, Z.Y., Mo, X.X., 2004. Origin of adakitic intrusives generated during mid-Miocene east–west extension in southern Tibet. Earth

Planet. Sci. Lett. 220 (1–2), 139–155.

Hou, Z.Q., Zeng, P.S., Gao, Y.F., Du, A.D., Fu, D.M., 2006. Himalayan Cu–Mo–Au mineralization in the eastern Indo-Asian collision zone: constraints from Re–Os dating of molybdenite. Mineral. Deposita 41, 33–45.

Hou, Z.Q., Zhang, H.R., Pan, X.F., Yang, Z.M., 2011. Porphyry Cu (–Mo–Au) deposits related to melting of thickened mafic lower crust: examples from the eastern Tethyan metallogenic domain. Ore Geol. Rev. 39 (1–2), 21–45.

Hou, Z.Q., Zheng, Y.C., Yang, Z.M., Rui, Z.Y., Zhao, Z.D., Jiang, S.H., Qu, X.M., Sun, Q.Z., 2013. Contribution of mantle components within juvenile lower-crust to collisional zone porphyry Cu systems in Tibet. Mineral. Deposita 48 (2), 173–192.

Hou, Z.Q, Yang, Z.M, Lu, Y.J, Kemp, A., Zheng, Y.C., Li, Q.Y., Tang, J.X, Yang, Z.S., Duan, L.F., 2015. A genetic linkage between subduction- and collision-related porphyry Cu deposits in continental collision zones. Geology 43(3), 247–250.

Hu, R.Z., Burnard, P.G., Bi, X.W., Zhou, M.F., Pen, J.T., Su, W.C., Wu, K.X., 2004. Helium and argon isotope geochemistry of alkaline intrusion-associated gold and copper deposits along the Red River-Jinshajiang fault belt, SW China. Chem. Geol. 203, 305.

Hu, Y.B., Liu, J.Q., Ling, M.X., Ding, W., Liu, Y., Zartman, R.E., Ma, X.F., Liu, D.Y., Zhang, C.C., Sun, S.J., Zhang, L.P., Wu, K., Sun, W.D., 2015. The formation of Qulong adakites and their relationship with porphyry copper deposit: geochemical constraints. Lithos 220–223, 60–80.

Hu, X., Garzanti, E., Moore, T., Raffi, I., 2015. Direct stratigraphic dating of India-Asia collision onset at the Selandian (middle Paleocene, 59±1Ma). Geology 43 (10), 859–862.

Huang, M.-L., Bi, X.-W., Gao, J.-F., Xu, L.-L., Xiao, J.-F., Liu, S.-T., Wang, X.-S., Zhoua, T., 2019. Sulfur and lead isotopic variations in the giant Yulong porphyry Cu (Mo-Au) deposit from the eastern Tibetan Plateau: implications for origins of S and Pb, and metal precipitation. J. Geochem. Explor. 197, 70–83.

Huang, M.L., Bi, X.W., Richards, J.P., Hu, R.Z., Xu, L.L., Gao, J.F., Zhu, J.J., Zhang, X.C., 2019. High water contents of magmas and extensive fluid exsolution during the formation of the Yulong porphyry Cu-Mo deposit, eastern Tibet. Journal of Asian Earth Sciences 176, 168–183.

Jacobsen, S.B., Wasserburg, G.J., 1980. Sm-Nd isotopic evolution of chondrites. Earth and Planetary Science Letters 50, 139–155.

Jiang, Y.H., Jiang, S.Y., Ling, H.F., Dai, B.Z., 2006. Low-degree melting of a metasomatized lithospheric mantle for the origin of Cenozoic Yulong monzogranite-porphyry, east Tibet: Geochemical and Sr–Nd–Pb–Hf isotopic constraints. Earth Planet. Sci. Lett. 241 (3–4), 617–633.

Jugo, P.J., Luth, R.W., Richards, J.P., 2005. Experimental data on the speciation of sulfur as a function of oxygen fugacity in basaltic melts. Geochim. Cosmochim. Acta 69, 497–503.

Kemp, A.I., Hawkesworth, C.J., Paterson, B.A., Kinny, P.D., 2006. Episodic growth of the Gondwana supercontinent from hafnium and oxygen isotopes in zircon. Nature 439 (7076), 580–583.

Kempton, P.D., Harmon, R.S., 1992. Oxygen isotope evidence for large-scale hybridization of the lower crust during magmatic underplating. Geochim. Cosmochim. Acta 56 (3), 971–986.

Keto, L.S., Jacobsen, S.B., 1987. Nd and Sr isotopic variations of Early Paleozoic oceans. Earth Planet. Sci. Lett. 84, 27–41.

Leech, M.L., Singh, S., Jain, A.K., Klemperer, S.L., Manickavasagam, R.M., 2005. The onset of India–Asia continental collision: early, steep subduction required by the timing of UHP metamorphism in the western Himalaya. Earth Planet. Sci. Lett. 234 (1–2), 83–97.

Leng, C.B., Gao, J.F., Chen, W.T., Zhang, X.C., Tian, Z.D., Guo, J.H., 2018. Platinum-group elements, zircon Hf-O isotopes, and mineralogical constraints on magmatic evolution of the Pulang porphyry Cu-Au system, SW China. Gondwana Res. 62, 163–177.

Li, C., Zhai, Q.G., Chen, W., Dong, Y.S., Yu, J.J., 2007. Geochronology evidence of the closure of Longmu Co-Shuanghu suture, Qinghai-Tibet plateau: Ar-Ar and zircon SHRIMP geochronology from ophiolite and rhyolite in Guoganjianian. Acta Petrol. Sin. 23 (5), 911–918.

Li, X.H., Li, W.X., Wang, X.C., Li, Q.L., Liu, Y., Tang, G.Q., 2009. Role of mantle-derived magma in genesis of early Yanshanian granites in the Nanling Range, South China: in situ zircon Hf-O isotopic constraints. Sci. China Ser. D-Earth Sci. 52, 1262–1278.

Li, X.H., Long, W.G., Li, Q.L., Liu, Y., Zheng, Y.F., Yang, Y.H., Chamberlain, K.R., Wan, D.F., Guo, C.H., Wang, X.C., Tao, H., 2010. Penglai zircon megacrysts: a potential new working reference material for microbeam determination of Hf-O isotopes and U-Pb age. Geostand. Geoanal. Res. 34 (2), 117–134.

Li, J.X., Qin, K.Z., Li, G.M., Xiao, B., Chen, L., Zhao, J.X., 2011. Post-collisional ore-bearing adakitic porphyries from Gangdese porphyry copper belt, southern Tibet: melting of thickened juvenile arc lower crust. Lithos 126, 265–277.

Li, J.X., Qin, K.Z., Li, G.M., Cao, M.J., Xiao, B., Chen, L., Zhao, J.X., Evans, N.J., McInnes, B.I.A., 2012. Petrogenesis and thermal history of the Yulong porphyry copper deposit, Eastern Tibet: insights from U-Pb and U-Th/He dating, and zircon Hf isotope and trace element analysis. Mineral. Petrol. 105 (3–4), 201–221.

Li, X.H., Tang, G.Q., Gong, B., Yang, Y.H., Hou, K.J., Hu, Z.C., Li, Q.L., Liu, Y., Li, W.X., 2013. Qinghu zircon: a working reference for microbeam analysis of U-Pb age and Hf and O isotopes. Chin. Sci. Bull. 58 (36), 4647–4654.

Liang, H.Y., Campbell, I.H., Allen, C., Sun, W.D., Liu, C.Q., Yu, H.X., Xie, Y.W., Zhang, Y.Q., 2006. Zircon Ce^{4+}/Ce^{3+} ratios and ages for Yulong ore-bearing porphyries in eastern Tibet. Mineral. Deposita 41 (2), 152–159.

Liang, H.Y., Campbell, I.H., Allen, C.M., Sun,W.D., Yu, H.X., Xie, Y.W., Zhang, Y.Q., 2007. The age of the potassic alkaline igneous rocks along the Ailao Shan–Red River shear zone: implications for the onset age of left-lateral shearing. J. Geol. 115, 231–242.

Lin, B., Wang, L.Q., Tang, J.X., Song, Y., Cao, H.W., Baker, M.J., Zhang, L.J., Zhou, X., 2018. Geology, geochronology, geochemical characteristics and origin of Baomai porphyry Cu (Mo) deposit, Yulong Belt, Tibet. Ore Geol. Rev. 92, 186–204.

Locock, A.J., 2014. An Excel spreadsheet to classify chemical analyses of amphiboles following the IMA 2012 recommendations. Computers & Geosciences 62, 1–11.

Lu, Y.J., Kerrich, R., Kemp, A.I.S., McCuaig, T.C., Hou, Z.Q., Hart, C.J.R., Li, Z.X., Cawood, P.A., Bagas, L., Yang, Z.M., Cliff, J., Belousova, E.A., Jourdan, F., Evans, N.J., 2013. Intracontinental Eocene-Oligocene porphyry Cu mineral systems of Yunnan,Western Yangtze Craton, China: compositional characteristics, sources, and implications for continental collision metallogeny. Econ. Geol. 108, 1541–1576.

Lugmair, G.W., Marti, K., 1978. Lunar initial ^{143}Nd/^{144}Nd: Differential evolution of the lunar crust and mantle. Earth and Planetary Science Letters 39, 349–357.

Mao, M., Rukhlov, A.S., Rowins, S.M., Spence, J., Coogan, L.A., 2016. Apatite trace element compositions: a robust new tool for mineral exploration. Econ. Geol. 111, 1187–1222.

Martin, H., Smithies, R.H., Rapp, R., Moyen, J.F., Champion, D., 2005. An overview of adakite, tonalite–trondhjemite–granodiorite (TTG), and sanukitoid: relationships and some implications for crustal evolution. Lithos 79, 1–24.

Metcalfe, I., 2013. Gondwana dispersion and Asian accretion: tectonic and palaeogeographic evolution of eastern Tethys. Journal of Asian Earth-Sciences 66, 1–33.

Miller, C., Schuster, R., Klötzli, U., Frank, W., Purtscheller, F., 1999. Post-collisional potassic and ultrapotassic magmatism in SW Tibet: geochemical and Sr–Nd–Pb–O isotopic constraints for mantle source characteristics and petrogenesis. J. Petrol. 40, 1399–1424.

Mo, X.X., Hou, Z.Q., Niu, Y.L., Dong, G.C., Qu, X.M., Zhao, Z.D., Yang, Z.M., 2007. Mantle contributions to crustal thickening during continental collision: evidence from Cenozoic igneous rocks in southern Tibet. Lithos 96 (1), 225–242.

Mungall, J.E., 2002. Roasting the mantle: Slab melting and the genesis of major Au and Au-rich Cu deposits. Geology 30, 915–918.

Mutch, E.J.F., Blundy, J.D., Tattitch, B.C., Cooper, F.J., Brooker, R.A., 2016. An experimental study of amphibole stability in low-pressure granitic magmas and a revised Al-in-hornblende geobarometer. Contrib. Mineral. Petrol. 171, 85.

Pearce, J., 1996. Sources and settings of granitic rocks. Episodes 19, 120–125.

Poitrasson, F., Hanchar, J.M., Schaltegger, U., 2002. The current state and future of accessory mineral research. Chem. Geol. 191, 3–24.

Qi, L., Hu, J., Gregoire, D.C., 2000. Determination of trace elements in granites by inductively coupled plasma mass spectrometry. Talanta 51 (3), 507–513.

Richards, J.P., 2003. Tectono-magmatic precursors for porphyry Cu(Mo-Au) deposit formation. Econ. Geol. 98 (8), 1515–1533.

Richards, J.P., 2005. Cumulative factors in the generation of giant calc-alkaline porphyry Cu deposits. In: Porter, T.M. (Ed.), Super Porphyry Copper and Gold Deposits: A Global Perspective, 1. Porter Geoscience Consulting Publishing, Linden Park, South Australia, pp. 7–25.

Richards, J.P., 2009. Postsubduction porphyry Cu-Au and epithermal Au deposits: Products of remelting of subduction-modified lithosphere. Geology 37 (3), 247–250.

Richards, J.P., 2011. Magmatic to hydrothermal metal fluxes in convergent and collided margins. Ore Geol. Rev. 40 (1), 1–26.

Richards, J.P., 2015. The oxidation state, and sulfur and Cu contents of arc magmas: implications for metallogeny. Lithos 233, 27–45.

Richards, J.P., Kerrich, R., 2007. Special paper: adakite-like rocks: their diverse origins and questionable role in metallogenesis. Econ. Geol. 102, 537–576.

Ridolfi, F., Renzulli, A., 2012. Calcic amphiboles in calc-alkaline and alkaline magmas: thermobarometric and chemometric empirical equations valid up to 1130 metric and chemo. Contrib Mineral Petrol 163, 877–895.

Ridolfi, F., Renzulli, A., Puerini, M., 2010. Stability and chemical equilibrium of amphibole in calc-alkaline magmas: an overview, new thermobarometric formulations and application to subduction-related volcanoes. Contributions to Minerology and Petrology 160, 45–66.

Rohalach, B.D., Loucks, R.R., 2005. Multi-million-year cyclic ramp-up of volatiles in a lower-crustal magma reservoir trapped below the Tampakan copper–gold deposit by Mio–Pliocene crustal compression in the southern Philippines. In: Porter, T.M. (Ed.), Super Porphyry Copper & Gold Deposits—A Global Perspective, vol. 2. PCG Publishing, Adelaide, South Austria, pp. 369–407.

Rollison, R.H., 1993. Using Geochemical Data: Evaluation, Presentation, Interpretation: United Kingdom. Longman, 352 p.

Scherer, E., Münker, C., Mezger, K., 2001. Calibration of the lutetiumhafnium clock. Science 293, 683–687.

Seedorff, E., Dilles, J.H., Proffett J.M., Einaudi, M.T., Zurcher, L., Stavast, W.J.A., Johnson, D.A., Barton, M.D., 2005. Porphyry deposits: characteristics and origin of hypogene features. Economic Geology 100th Anniversary Volume, 251–298.

Shafiei, B., Haschke, M., Shahabpour, J., 2009. Recycling of orogenic arc crust triggers porphyry Cu mineralization in Kerman Cenozoic arc rocks, southeastern Iran. Mineral. Deposita 44 (3), 265–283.

Sillitoe, R.H., 1972. A plate tectonic model for the origin of porphyry copper deposits. Econ. Geol. 67 (2), 184–197.

Sillitoe, R.H., 2010. Porphyry Copper Systems. Econ. Geol. 105 (1), 3–41.

Singer, B.S., Dungan, M., Layne, G.D., 1995. Textures and Sr, Ba, Mg, Fe, K, and Ti compositional profiles in volcanic plagioclase: clues to the dynamics of calc-alkaline magma chambers. Am. Mineral. 80, 776–798.

Spurlin, M.S., Yin, A., Horton, B.K., Zhou, J., Wang, J., 2005. Structural evolution of the Yushu–Nangqian region and its relationship to syncollisional igneous activity,

eastcentral Tibet. Geol. Soc. Am. Bull. 117, 1293–1317.

Steiger, R.H., Jäger, E., 1977. Subcommission on geochronology: convention on the use of decay constants in geo- and cosmochronology. Earth Planet. Sci. Lett. 36, 359–362.

Streck, M.J., Dilles, J.H., 1998. Sulfur evolution of oxidized arc magmas as recorded in apatite from a porphyry copper batholith. Geology 26, 523–526.

Sun, S.S., McDonough, W.F., 1989. Chemical and Isotopic Systematics of Oceanic Basalts: Implication for Mantle Composition and Processes, 42. Geological Society Special Publication, pp. 313–345.

Tang, R.L., Luo, H.S., 1995. The geology of Yulong Porphyry Copper (Molybdenum) Ore Belt, Xizang (Tibet): Beijing, 320. Geological Publishing House (in Chinese).

Tibet Yulong Copper Co., Ltd., 2009. Yulong Copper Polymetallic Deposit Exploration Report. Jomda County, Tibet.

Ustunisik, G., Kilinc, A., Nielsen, R.L., 2014. New insights into the processes controlling compositional zoning in plagioclase. Lithos 200, 80–93.

Valley, J.W., Kinny, P.D., Schulze, D.J., Spicuzza, M.J., 1998. Zircon megacrysts from kimberlite: oxygen isotope variability among mantle melts. Contrib. Mineral. Petrol. 133 (1–2), 1–11.

Valley, J.W., Lackey, J.S., Cavosie, A.J., Clechenko, C.C., Spicuzza, M.J., Basei, M.A.S., Bindeman, I.N., Ferreira, V.P., Sial, A.N., King, E.M., Peck, W.H., Sinha, A.K., Wei, C.S., 2005. 4.4 billion years of crustal maturation: oxygen isotope ratios of magmatic zircon. Contrib. Mineral. Petrol. 150 (6), 561–580.

Wang, J.H., Yin, A., Harrison, T.M., Grove, M., Zhang, Y.Q., Xie, G.H., 2001. A tectonic model for Cenozoic igneous activities in the eastern Indo-Asian collision zone. Earth Planet. Sci. Lett. 88, 123–133.

Wang, Q., Xu, J.F., Jian, P., Bao, Z.W., Zhao, Z.H., Li, C.F., Xiong, X.L., Ma, J.L., 2006. Petrogenesis of adakitic porphyries in an extensional tectonic setting, Dexing, South China: implications for the genesis of porphyry copper mineralization. J. Petrol. 47, 119–144.

Wang, C.H., Tang, J.X., Chen, J.P., Hao, J.H., Gao, Y.M., Liu, Y.W., Fan, T., Zhang, Q.Z., Ying, L.J., Chen, Z.J., 2009. Chronological research of Yulong Copper-Molybdenum porphyry deposit. Acta Geol. Sin. 83, 1445–1455 (in Chinese with English abstract).

Wang, C.H., Tang, J.X., Hou, K.J., Gao, Y.M., Chen, J.P., Hao, J.H., Ying, L.J., Zhang, Q.Z., Liu, Y.W., Fan, T., 2011. Hf isotopic characteristics of Yulong copper-molybdenum porphyry deposit in Tibet and their geological significance. Mineral Deposits 30, 292–304 (in Chinese with English abstract).

Wang, R., Richards, J.P., Hou, Z.Q., Yang, Z.M., 2014. Extent of underthrusting of the Indian plate beneath Tibet controlled of Miocene porphyry Cu–Mo±Au deposits. Mineral. Deposita 49, 165–173.

Wang, R., Weinberg, R.F., Collins, W.J., Richards, J.P., Zhu, D.C., 2018. Origin of post–collisional magmas and formation of porphyry Cu deposits in southern Tibet. Earth Sci. Rev. 181, 122–143.

Waters, L.E., Lange, R.A., 2015. An updated calibration of the plagioclase-liquid hygrometer-thermometer applicable to basalts through rhyolites. Am. Mineral. 100, 2172–2184.

Wiedenbeck, M., Hanchar, J.M., Peck, W.H., Sylvester, P., Valley, J., Whitehouse, M., Kronz, A., Morishita, Y., Nasdala, L., Fiebig, J., Franchi, I., Girard, J.P., Greenwood, R.C., Hinton, R., Kita, N., Mason, P.R.D., Norman, M., Ogasawara, M., Piccoli, R., Rhede, D., Satoh, H., Schulz-Dobrick, B., Skar, O., Spicuzza, M.J., Terada, K., Tindle, A., Togashi, S., Vennemann, T., Xie, Q., Zheng, Y.F., 2004. Further characterisation of the 91500 zircon crystal. Geostand. Geoanal. Res. 28, 9–39.

Winchester, J.A., Floyd, P.A., 1977. Geochemical discrimination of different magma series and their differentiation products using immobile elements. Chem. Geol.

20, 325–343.

Woodhead, J., Hergt, J., Shelley, M., Eggins, S., Kemp, R., 2004. Zircon Hf-isotope analysis with an excimer laser, depth profiling, ablation of complex geometries, and concomitant age estimation. Chem. Geol. 209, 121–135.

Wu, F.Y., Yang, Y.H., Xie, L.W., Yang, J.H., Xu, P., 2006. Hf isotopic compositions of the standard zircons and baddeleyites used in U-Pb geochronology. Chem. Geol. 234, 105–126.

Wu, T., Xiao, L., Ma, C.Q., Huang, Q., 2013. The geochronological, geochemical and Sr-Nd isotopic characteristics of the Tongpu intrusive complex and its implications. Acta Petrol. Sin. 29, 3567–3580.

Xu, L.L., Bi, X.W., Hu, R.Z., Zhang, X.C., Su, W.C., Qu, W.J., Hu, Z.C., Tang, Y.Y., 2012. Relationships between porphyry Cu–Mo mineralization in the Jinshajiang–Red River metallogenic belt and tectonic activity: constraints from zircon U–Pb and molybdenite Re–Os geochronology. Ore Geol. Rev. 48, 460–473.

Xu, L.L., Bi, X.W., Hu, R.Z., Qi, Y.Q., Tang, Y.Y., Wang, X.S., Zhu, J.J., 2016. Redox states and genesis of magmas associated with intra-continental porphyry Cu–Au mineralization within the Jinshajiang–Red River alkaline igneous belt, SW China. Ore Geol. Rev. 73, 330–345.

Xu, L.L., Bi, X.W., Hu, R.Z., Tang, Y.Y., Wang, X.S., Huang, M.L., Wang, Y.J., Ma, R., Liu, G., 2016. Contrasting whole-rock and mineral compositions of ore-bearing (Tongchang) and ore-barren (Shilicun) granitic plutons in SW China: Implications for petrogenesis and ore genesis. Lithos 336–337, 54–66.

Yang, Y.H., Wu, F.Y., Wilde, S.A., Liu, X.M., Zhang, Y.B., Xie, L.W., Yang, J.H., 2009. In situ perovskite Sr–Nd isotopic constraints on the petrogenesis of the Ordovician Mengyin kimberlites in the North China Craton. Chem. Geol. 264, 24–42.

Yang, Z.M., Hou, Z.Q., Xu, J.F., Bian, X.F., Wang, G.R., Yang, Z.S., Tian, S.H., Liu, Y.C., Wang, Z.L., 2014. Geology and origin of the post-collisional Narigongma porphyry Cu–Mo deposit, southern Qinghai, Tibet. Gondwana Res. 26 (2), 536–556.

Yang, Y.H., Wu, F.Y., Yang, J.H., Chew, D.M., Xie, L.W., Chu, Z.Y., Zhang, Y.B., Huang, C., 2014. Sr and Nd isotopic compositions of apatite reference materials used in U-Th–Pb geochronology. Chem. Geol. 385, 35–55.

Yang, L., Wang, Q.F., Wang, Y.M., Li, G.J., 2018. Proto- to Paleo-Tethyan evolution of the eastern margin of Simao block. Gondwana Res. 62, 61–74.

Zhang, Y.Q., Xie, Y.W., 1997. Geochronology of Ailaoshan-Jinshajiang alkalirich intrusive rocks and their Sr and Nd isotopic characteristics. Science China Earth Sciences 40 (5), 524–529.

Zhang, Y.Q., Xie, Y.W., Qiu, H.N., Li, X.H., Chung, S.L., 1998. Shoshonitic series: Geochemical characteristics of elements for ore-bearing porphyry from Yulong copper ore belt in eastern Tibet. Earth Science-Journal of China University of Geosciences 23, 557–561 (in Chinese with English abstract).

Zhu, J.J., Hu, R.Z., Bi, X.W., Zhong, H., Chen, H., 2011. Zircon U-Pb ages, Hf-O isotopes and whole-rock Sr-Nd-Pb isotopic geochemistry of granitoids in the Jinshajiang suture zone, SW China: Constraints on petrogenesis and tectonic evolution of the Paleo-Tethys Ocean. Lithos 126, 248–264.

Zhu, J.J., Richards, J.P., Rees, C., Creaser, R., DuFrane, S.A., Locock, A., Petrus, J.A., Lang, J., 2018. Elevated Magmatic Sulfur and Chlorine Contents in Ore-Forming Magmas at the Red Chris Porphyry Cu-Au Deposit, Northern British Columbia, Canada. Econ. Geol. 113 (5), 1047–1075.

Zi, J.W., Cawood, P.A., Fan, W.M., Wang, Y.J., Tohver, E., Mccuaig, T.C., Peng, T.P., 2012. Triassic collision in the Paleo-Tethys Ocean constrained by volcanic activity in SW China. Lithos 144-145 (7), 145–160.

Zi, J.W., Cawood, P.A., Fan, W.M., Wang, Y.J., Eric, T., 2012. Contrasting rift and subduction-related plagiogranites in the Jinshajiang ophiolitic mélange, southwest China, and implications for the Paleo-Tethys. Tectonics 31, TC2012.